



**CHALMERS**  
UNIVERSITY OF TECHNOLOGY

---

# Surface impact of wet and dry agglomerates

Master's thesis in Innovative and Sustainable Chemical Engineering

JOAKIM OLSSON

---

Department of Chemistry and Chemical Engineering

CHALMERS UNIVERSITY OF TECHNOLOGY

Gothenburg, Sweden 2017



Surface impact of wet and dry agglomerates

Joakim Olsson

© JOAKIM OLSSON, 2017

Department of Chemistry and Chemical Engineering

Chemical Engineering

SE- 412 96 Gothenburg

Sweden

Telephone: +46 (0) 31 772 43 90

## Abstract

The wall normal impact of wet and dry, polydisperse agglomerates was simulated in the DEM software LIGGGHTS. Assuming the pulling of liquid bridges at impact is rapid, thermodynamic equilibrium is not attained and their volume is approximately constant. A DEM model with equations describing the static and dynamic parts of the capillary force exerted by a liquid bridge between two particles and a particle and wall with a constant volume liquid bridge was implemented. Particles were found to have large interface energies and calculation of the dimensionless Tabor number showed that the JKR theory is suitable for modelling the adhesive contact forces of dry agglomerates. The adhesive forces were assumed negligible in wet agglomerates and contact forces were modelled using the Hertz theory. Impact behaviour was analyzed through damage ratio, total fragmentation, capture ratio and total adhesion force. In the analysis of impact behaviour four impact regimes were identified and they were found to be best distinguished by the total number of fragmented particles. The impact behaviour is universalized by the creation of a regime map based on agglomerate liquid content and the dimensionless number  $\Delta$ , which is a measure of the agglomerate strength.

**Keywords:** Discrete element method, Capillary force, Pendular liquid bridge, Regime map, Wet agglomerate impact

## **Acknowledgements**

I want to thank my thesis supervisor PhD Mohammad Khalilitehrani for believing in me and encouraging me throughout this thesis. I would also like to thank Professor Anders Rasmuson for his guidance and fruitful discussions. I am grateful to all the colleagues and fellow master students at the division of Chemical Engineering who made my time there a great experience.

Finally, I would like to thank my family for their support and continuous encouragement throughout my years of study and during the thesis work. I could not have made it without them.

Thank you.

## Nomenclature

$a$	Contact area radius	[m]
$a_0$	Equilibrium contact area radius	[m]
$A_H$	Hamaker constant	[J]
$c$	Characteristic	
$D_o$	Equilibrium separation distance	[m]
$e$	Restitution coefficient	[-]
eff	effective	
$E$	Young's modulus	[GPa]
$f$	flat	
$G$	Shear modulus	[Pa]
$H$	Interparticle separation distance	[m]
$I$	Moment of inertia	[kg/m <sup>2</sup> ]
$k$	spring constant	[N/m]
$m$	mass	[kg]
$N$	Number of bonds	
$n$	normal	
$R, r$	Radius	[m]
$U$	energy	[J]
$v$	Vapor	
$V$	Volume	[m <sup>3</sup> ]
$x$	Spring displacement	[m]
$W$	Work of adhesion	[J/m <sup>2</sup> ]

## Subscripts

ID	Identified specific pairwise initial bonds
l	Liquid
lb	Liquid bridge
lv	Liquid-Vapor
p	Particle
o	Original, at time zero
s	Solid
sl	Solid-Liquid
sppl	Sphere-Plate
spsp	Sphere-Sphere
sv	Vapor-Solid
t	tangential

## Greeks

$\alpha$	Half-filling angle	[°]
$\gamma$	Surface tension	[N/m]
$\Delta$	delta number	[-]
$\delta$	overlap	[m]
$\eta$	damping coefficient	[Ns/m]
$\theta$	Contact angle	[°]
$\nu$	Poisson's ratio	[-]
$\mu$	Viscosity	[Pas]
$\omega$	angular velocity	[rad/s]

# Table of content

1. Introduction.....	1
1.1 Background.....	1
1.2 Objective.....	4
2. Theoretical background.....	5
2.1 The Discrete Element Method.....	5
2.1.1 Hertz contact theory.....	7
2.1.2 Adhesive elastic contacts.....	9
2.2 Wet granular matter.....	10
2.2.1 Pendular liquid bridges and capillary forces.....	11
2.2.2 Capillary forces in DEM.....	13
2.2.3 Liquid bridge formation distance.....	19
2.2.4 Liquid bridge rupture distance.....	20
2.2.5 Liquid distribution at rupture.....	21
2.2.6 Dynamic liquid bridge forces.....	22
3. Methodology.....	23
3.1 Material properties.....	23
3.1.1 Elastic mechanical properties.....	23
3.1.2 Capillary force properties.....	24
3.1.3 Particle size distribution.....	25
3.2 Agglomerate liquid content.....	27
3.3 DEM implementation.....	27
3.3.1 Contact force modelling.....	27
3.3.2 Capillary force modelling.....	28
3.3.3 Simulation time step.....	30
3.3.4 Agglomerate formation.....	31

3.3.5	Characterisation.....	32
3.4	Wall normal impact procedure .....	33
3.5	Post processing .....	34
3.5.1	Damage ratio .....	34
3.5.2	Initial bonds broken.....	34
3.5.3	Wall adhesion.....	35
3.5.4	Capture ratio.....	35
3.5.5	Total adhesive force .....	35
3.5.6	Fragmentation.....	36
3.5.7	Regime map.....	37
4.	Results and discussion .....	39
4.1	Impact regimes .....	39
4.1.1	Minor deformation .....	39
4.1.2	Major deformation, Minor fragmentation .....	40
4.1.3	Major deformation, Major fragmentation .....	40
4.1.4	Disintegration .....	41
4.2	Compactability and deformability .....	41
4.3	Total fragmentation .....	44
4.4	Agglomerate-wall adhesion.....	45
4.5	Regime map.....	47
4.6	Reflections .....	48
5.	Conclusions.....	49
6.	Suggestions for further work.....	50
	References .....	51
	Appendix A .....	56
	Appendix A.1.....	56

Appendix A.2.....	57
Appendix A.3.....	58

# 1. Introduction

Active safety systems are crucial tools for mitigating accidents on roads and are getting more complex and wide-spread. Such systems include a variety of complementary sensors including cameras, Lidars, radars and ultrasound sensors enabling a 360-degree view at all instants. However, the ability of these sensors is easily impaired by accumulation of contaminants on to the surfaces blocking their view. Efficient cleaning systems are therefore vital to secure effective use of the active safety systems, especially in respect to autonomous vehicles. Depending on climate and road conditions there is a variety of possible contaminants, among which the most common are snow, dirt suspensions and solid dirt particles. There are three general mechanisms of soiling, i.e. the transportation of contaminants to vehicle exterior surface: (1) it may be blown onto the surface by winds, (2) it may be stirred up from the wheels of the vehicle driving in front or (3) it may be stirred up from the vehicles own wheels (Hagemeier, 2011)

Plenty of researches have been conducted on modelling of car exterior contamination via water and droplet soiling (Gaylard, 2017), (Hagemeier 2011). However, little has been done on contamination by solid dirt particles. Contamination of solid particles may occur via impact of single particles or large formations of particles bound together in an agglomerate. To the authors knowledge, no research has been done on the contamination by agglomerates. Surface cleaning properties of agglomerate impact is dependent on the impact behaviour, which affects the extent of fragmentation and agglomerate-surface adhesion force. Previous work on single solid dirt particle contamination have applied a sticking boundary condition for any particle impacting a surface (Yoshida, 1998). The impact behaviour of the agglomerate is dependent on several parameters, such as for example impact velocity, agglomerate moisture content, size distribution, etc. Creation of better predictive models of agglomerate impact behaviour are therefore of interest for the development of more effective cleaning systems.

## 1.1 Background

When many smaller particles begin to adhere to each other they can form a larger structure called agglomerate. There are several intermolecular forces providing the necessary adhesive force for the formation of such structures, e.g. van der Waals forces, chemical bonds,

electrostatic charges, or liquid bridge forces. Van der Waals forces are generally negligible for larger macroscopic bodies due to the large dependence on interparticle separation distance. However, with decreasing particle size ( $\sim 10 \mu\text{m}$ ) the force can become large enough to form dry agglomerates (Li, 2004). Another important force for the formation of agglomerates is the capillary force. Even the slightest humidity is enough to increase the adhesion of particles due to capillary condensation of vapor in the pores of the contact surfaces between particles (Mitarai and Nori, 2006). Agglomeration is an important phenomenon in industrial powder processing. In pharmaceutical industries, agglomeration of powder is done in a deliberate and controlled manner to improve powder flow properties, reduce dust formation and prevent particle segregation (Shanmugam, 2015), (Thornton & Liu, 2004). Typically, agglomerates are formed by wet granulation in which a liquid binder is added to enhance agglomeration by capillary force, or by dry granulation in which agglomerates are formed by van der Waals forces during compression of the powder. In subsequent processing of the agglomerate powder, agglomerates may collide for example with each other or with a flat surface, and break in to fragments or coalesce in to larger structures. Prediction of the collisional behaviour of agglomerates is therefore of interest in variety of applications.

Granular materials such as agglomerates can be modelled on a microscale by considering the collision and interactions of every single particle in the structure. Elastic collisions between particles are commonly modelled by the hard sphere approach or the soft sphere approach (Crowe, 2011). In the hard-sphere approach collisions are assumed to be binary and instantaneous such that the collision can be calculated through the integral form of Newton's 2<sup>nd</sup> law of motion. Post collision velocities are then determined by simple relations between the pre-impact velocities and the coefficient of restitution and the coefficient of friction (Crowe, 2011). The low numerical burden of this method is attractive; however, the underlying assumptions of instantaneous collisions makes it unsuitable for modelling dense granular matter (Crowe, 2011). A more suitable model is the soft-sphere approach, generally referred to as the discrete element method, DEM. It was developed by Cundall and Strack (1978) to simulate assemblies of discs and spheres for studying soil mechanics. In difference to the hard sphere approach, this approach acknowledges that in any real collision deformation of the bodies will occur. Deformation is modelled by allowing particles, which are assumed to be rigid bodies, to overlap. Contact forces can then be related to size of the overlap and calculated as a spring-

dashpot system. Newton's 2<sup>nd</sup> law of motion is then solved by numerical integration through which position, velocity and forces acting on each particle is calculated throughout the duration of collisional contact. Because the simulation time steps must be small enough to resolve the collisions DEM is computationally heavier than the hard-sphere approach (Crowe, 2011). For accurate simulation of particle deformation during collision the finite element method can be used. The DEM simulation can be coupled with FEM to resolve the deformation; however, the computational burden can become unfeasible with increasing number of particles (Kruggel-Emden, 2007).

There is a strong body of knowledge on modelling and simulation of dry granular matter using DEM (Thornton, 2015). It has been found to be a useful tool in simulations of soil mechanics (Shamy and Gröger, 2008), dry granulation in high-shear mixers (Tamadondar et al, 2017), silo discharge and several other powder processing units (Ketterhagen, 2009). Contact forces exerted between overlapping particles is typically modelled by either Hertz or Johnson, Kendall and Robert (JKR) theory. Johnson et.al (1971) acknowledged that the Hertz contact theory fails to account for the effect of adhesion on the contact area, rendering it inapplicable for particle interaction in which adhesive forces are significant. Based on the Hertz contact theory Johnson (1971) derived a new model, the JKR theory, that was more accurately describing adhesive interactions. Implementation of this contact model was performed by Nguyen et al (2014) in the DEM software LIGGGHTs for the simulation of dry, monodisperse agglomerates impacting a single, larger particle.

Modelling of wet granular matter on the other hand is more complex and DEM simulations of agglomerates is far scarcer than those of dry. The general problem is that fluid phases are explicitly neglected in the DEM framework, only Newton's 2<sup>nd</sup> law of motion for solid particles is solved. Any fluid force acting on the particles must either be modelled by available simulation parameters or the simulation be coupled to CFD simulations determining the interstitial fluid movement and forces as described by Kloss (2012). The interstitial fluid in a wet granular material has been found to follow four different regimes. Depending on the degree of liquid saturation the regimes are labelled pendular, funicular, capillary or droplet (Mitarai & Nori, 2006). For very small liquid contents, the pendular regime applies and interstitial liquid is found as discrete pendular bridges between particles pairs. Calculation of the capillary force exerted

by liquid bridges requires information on the radius of curvature of the bridge. For a liquid bridge in thermodynamic equilibrium the curvature is described by the Young-Laplace equation, a second order non-linear differential equation to which, in general no analytical solution exists (Lambert & Valsamis, 2013). Unless simplifications are made, numerical integration is necessary to determine the force and the term exact solution refers to the numerical integration of the Young-Laplace equation (Lian, 1993). The exact solution is computationally heavy to implement in the DEM framework and simplified methods must be applied. Capillary force models have for example been implemented via look up tables of the exact solution calculated a priori (Shi & McCarthy, 2008), regression models of the exact solution (Mikami, 1998) and by approximated closed form equations in which the force is determined through explicit functions of bridge volume and separation distance (Lian, 1998). Rabinovitch. (2005) developed closed form equations under the assumption of small, constant volume bridges, as opposed to the previously described case of thermodynamic equilibrium where volume is determined by the vapor pressure. Constant bridge volume is typically assigned non-volatile liquids such as oil or when rapid pulling of the bridge is expected (Butt, 2010). At impact of agglomerates, the pulling of the liquid bridges is expected to be fast such that thermodynamic equilibrium is not obtained and the volume is approximately constant.

## **1.2 Objective**

The objective of this thesis is to develop a regime map of the normal impact behaviour of wet and dry polydisperse agglomerates. This entails the implementation of DEM models for simulating wet and dry agglomerates. In more detail, the aim is to implement suitable models for calculation of the capillary force in pendular liquid bridges between polydisperse particles. The effect of liquid content on post impact behaviour will be investigated and a regime map will be created.

## 2. Theoretical background

Adhesive van der Waals forces between particles are relatively large and the dry agglomerates are simulated using the JKR contact theory. Because the van der Waals forces is reduced by approximately one order of magnitude when liquid is introduced on the surface, in case of wet contacts, the van der Waals force is neglected and Hertz contact theory is used. In calculation of the capillary force through a pendular liquid bridge, there exists two possible thermodynamic cases. In the first case, the bridge is in thermodynamic equilibrium with the surrounding vapor such that the volume and radius of curvature of the bridge is determined by the vapor-liquid equilibrium. The second case is that of non-equilibrium liquid bridges in which case, the volume of the bridge is constant and the radius is a function of the particle-particle separation distance and bridge volume. The constant volume bridge assumption applies for non-volatile liquids or when the bridge is stretched or compressed rapidly. In the case of impact between an agglomerate and a wall as is to be studied in this thesis, pulling of the bridges is assumed to be fast and the bridge is not in equilibrium with the surroundings. Closed form approximations derived for constant volume bridges are therefore used to model the capillary force in the impact of wet agglomerates. In the following part of this section the discrete element method and its application in modelling of dry granular matter will be introduced. This is followed by an overview of theory on static and dynamic forces of pendular liquid bridges. Important aspects such as critical rupture distance, formation distance and force models for pendular liquid bridges will be discussed as accuracy of this modelling is vital for the DEM model.

### 2.1 The Discrete Element Method

In the collision between two solid particles, or a particle and wall, the bodies will deform and exert a repulsive force on each other. Impact of a single particle and its deformation can be simulated with a continuum approach using the finite element method, However, as the number of particles increase the computational burden can become unfeasible for modelling granular matter. A more suitable method for simulating dense granular materials is the discrete element method, DEM. It was developed by Cundall and Strack (1979) to simulate the mechanical behaviour of assemblies of discs and spheres with application to soil and rock mechanics. Assuming particles to be spherical rigid bodies, interacting only at point contact, the deformation is modelled by allowing particles to overlap as shown in Figure 2:1.

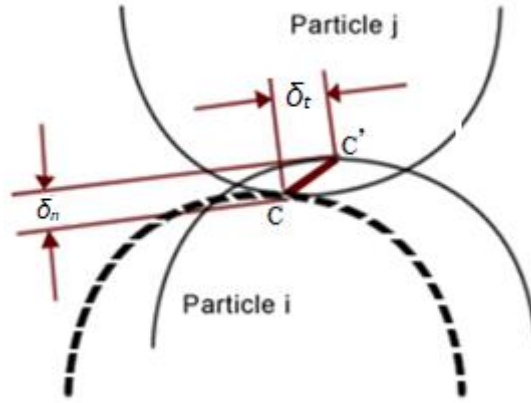


Figure 2:1. Normal ( $\delta_n$ ) and tangential ( $\delta_t$ ) overlap between to particles  $i$  and  $j$ . Particles are colliding obliquely and particle  $i$  at moment of contact is shown by the dotted line and solid line show is particle  $i$  at some time after contact.  $C$  is the point of contact at first moment of contact and  $C'$  is the point of contact at some time after.

Furthermore, it assumed that the size of the overlap is negligible compared to the radius of the particles. Simulation time step is supposed to be small enough that force disturbances do not propagate further than to any particle in immediate contact. As a consequence, all interactions are considered independent of each other and the total force acting on particle A is the sum of the interaction forces between particle A and particles in contact with A.

With the previous assumptions, the contact force between two particles can be calculated as a function of the size of the overlap. Newton's 2<sup>nd</sup> law of motion is then solved by numerical integration for every individual particle in the system according to equations 1 and 2:

$$m_i \frac{d^2 x_i}{dt^2} = \sum_j F_{contact}^{ij} + F_{gravity}^i + F_{fluid}^i + F_{drag}^i + \dots \quad (1)$$

$$I_i \frac{d\omega_i}{dt} = T_{contact}^i \quad (2)$$

where  $m_i$ ,  $x_i$  are the mass and position of particle  $i$ ,  $t$  is time and  $I_i$ ,  $\omega_i$ ,  $T_{contact}^i$  are the moment of inertia, angular velocity and the torque exerted on particle  $i$  respectively. In equation 1,  $F_{Contact}^{ij}$  is the force related to the particle-particle contacts as determined by their overlap,  $F_{gravity}^i$  is the gravity force,  $F_{fluid}^i$  is the force exerted on particle  $i$  by the surrounding fluid (including pressure and buoyancy forces) and  $F_{drag}^i$  is the drag force. Any other force acting

on the particle could be added to the right side of equation 1, such as Capillary, Brownian, Thermophoretic, Basset force, history force etc. In this thesis, all forces except contact forces and capillary forces will be neglected. Theory and implementation of the capillary force will be explained in Chapter 2.2.

The repulsive force between particles due to the deformation can be modelled as the compression of a spring with equilibrium position at zero deformation (Crowe., 2011). Increased deformation, results in an increased potential energy stored in the spring and thus increased repulsive force between the particles. In fully elastic collisions the spring returns to its equilibrium position without any loss of energy during compression and decompression. In any real impact energy losses will inevitably occur through different mechanisms such as viscous dissipation or plastic deformation (Krijt., 2013). Viscous energy dissipation is a function of the relative velocities of colliding particles and can be modelled by a viscous damper, or dashpot, (Crowe, 2011). The particle-particle contact force interaction is then described by the equation of motion of a spring-dashpot system as shown in equation 3:

$$m\ddot{x} + \eta\dot{x} + kx = 0 \quad (3)$$

where  $m$  is the mass of the particle,  $\eta$  is the damping coefficient,  $k$  is the spring stiffness constant and  $x$  is the overlap. The force acting on a particle is divided into a normal force and a tangential force, each of which can be determined by a spring-dashpot system such as that in equation 3 (Crowe, 2011). The spring stiffness and damping coefficients can be related to material properties through different equations depending on the contact theory used (Thornton, 2015). Which contact force theory to use is in turn dependent on the material properties of the interacting bodies. Two well-known theories of contact mechanics are Hertz and JKR. Hertz theory is applicable for non-adhesive interactions as it does not take in to account adhesive forces (Lian, 2011). The JKR theory is derived from the Hertz theory while including the effect of adhesion on the interaction such that it can be applied for adhesive interactions (Li, 2011)

### **2.1.1 Hertz contact theory**

In Hertz contact theory, particles are assumed non-cohesive and interaction can only occur on a contact area created by deformation of particles that is much smaller than the particle radius.

Contact forces between two particles in an elastic collision is decomposed into two parts, elastic and damping, as described earlier by the spring-dashpot system. It is found that the relationship between normal force and overlap is nonlinear, unlike the linear equation 3. In Hertz contact theory, overlap is raised to the power 3/2 (Crowe, 2011) and the elastic force is given by equations 4 and 5:

$$F_{ne} = \frac{4}{3}E_{eff}\sqrt{R_{eff}\delta_{n,ij}} \delta_{n,ij} \quad (4)$$

$$F_{te} = 8G_{eff}\sqrt{R_{eff}\delta_{n,ij}} \delta_{n,ij} \quad (5)$$

In equation 4 and 5 are  $F_{ne}$ ,  $F_{te}$  the normal and tangential damping forces,  $E_{eff}$  the effective Young's modulus,  $G_{eff}$  the effective shear modulus,  $R_{eff}$  the effective radius  $R_{eff} = \left(\frac{1}{R_i} + \frac{1}{R_j}\right)^{-1}$  and  $\delta_{n,ij}$  the normal overlap. The damping part is a function of the restitution coefficient as expressed by Mindlin (1949) and is given by equations 6-9:

$$F_{nd} = -2\sqrt{\frac{5}{6}}\frac{\ln(e)}{\sqrt{\ln^2(e)+\pi^2}}\sqrt{S_n m_{eff}} (v_{n,ij}) \quad (6)$$

$$F_{td} = -2\sqrt{\frac{5}{6}}\beta\sqrt{S_t m_{eff}} (v_{t,ij}) \quad (7)$$

where

$$S_n = 2E_{eff}\sqrt{R_{eff}\delta_{N,ij}} \quad (8)$$

$$S_t = 8G\sqrt{R_{eff}\delta_{N,ij}} \quad (9)$$

where  $F_{nd}$ ,  $F_{td}$  are normal and tangential damping forces,  $S_n, S_t$  are normal and shear stiffnesses;  $m_{eff}$  is the effective mass and  $v_{n,ij}$ ,  $v_{t,ij}$  are the normal and tangential relative velocity of the interacting particles. In equation 3-8,  $E$  and  $G$  are effective Young and shear modulus in a contact and are given by equations 10 and 11:

$$\frac{1}{E_{eff}} = \frac{1-v_i^2}{E_i} + \frac{1-v_j^2}{E_j} \quad (10)$$

$$\frac{1}{G_{eff}} = \frac{2(2+v_i)(1-v_i)}{E_i} + \frac{2(2+v_j)(1-v_j)}{E_j} \quad (11)$$

In equations 10 and 11,  $\nu_i$  is the Poisson's ratio of particle  $i$ .

## 2.1.2 Adhesive elastic contacts

There are two common models for elastic-adhesive contact forces, the “DMT” (Derjaguin, 1975) and “JKR” (Johnson, 1971) theories. DMT theory assumes the contact area to be independent of the adhesive Van der Waals force. Adhesion is incorporated by the addition of a constant positive force to the normal Hertz elastic force (Li, 2011). As such, the DMT treats adhesive interactions as the Hertz elastic contact shifted by a constant force. In JKR theory adhesive forces is not merely a constant additional term. Instead, adhesive and elastic forces can interact and affect the contact area. Because of adhesion, the contact area obtained by JKR for a given force is greater than the corresponding Hertz contact area. Which model to choose for a given system can be determined by the value of a dimensionless number called the Tabor number ( $\mu$ ), which is a measure of the magnitude of elastic deformation to the adhesive forces (Tabor, 1977). DMT is suitable for systems with low Tabor number ( $\mu < 0.1$ ) while JKR is better suited for larger Tabor numbers ( $\mu > 3.0$ ) (Li, 2011).

Elastic contacts between particles described by JKR is characterized by a contact radius which is a function of both elastic properties of the solid particles and the surface energies (Johnson, 1971):

$$a^3 = \frac{3R_{eff}}{4E_{eff}} [F_{ne} + 3\pi W_{ij} R_{eff} + \sqrt{6\pi W_{ij} R_{eff} F_{ne} + (3\pi W_{ij} R_{eff})^2}] \quad (12)$$

In this equation  $F_{ne}$  is the normal elastic-adhesive force. The normal elastic adhesive force,  $F_{ne}$ , can be expressed as a function of the contact radius and the particle overlap through equation 13 (Chokshi, 1993):

$$\frac{F_{ne}}{F_{PO}} = 4 \left( \frac{a}{a_0} \right)^3 - 4 \left( \frac{a}{a_0} \right)^{\frac{3}{2}} \quad (13)$$

where  $F_{PO}$  is the critical force, or pull-off force, that occurs at the critical overlap and  $a_0$  is the equilibrium contact area. Considering the interaction between two adhesive particles without any external force acting on them, adhesive surface forces will pull the bodies together such that at mechanical equilibrium a contact area, the equilibrium contact area, is kept in the

deformed contact region between them. At this moment surfaces exert the maximum adhesive force, corresponding to the maximum tensile force required to break the contact which is known as the pull-off force (Johnson, 1971). These two parameters are calculated by equations 14,15.

$$F_{PO} = \frac{3}{2} W_{ij} \pi R_{eff} \quad (14)$$

$$a_0 = \left( \frac{9 W_{ij} \pi R_{eff}^2}{2 E_{eff}} \right) \quad (15)$$

Due to the adhesive forces pulling the particles surfaces together contacts are kept intact over a finite separation distance as shown in Figure 2:2. This phenomenon is known as necking and contacts will break when the separation distance exceeds a certain critical, negative, overlap.

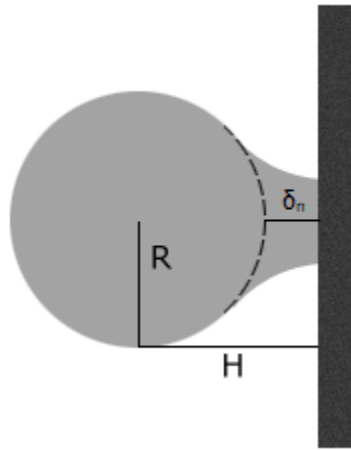


Figure 2:2 A particle with radius  $R$  experiencing necking. The separation distance  $H$  is greater than the radius and there is negative overlap  $\delta_n$ . The dashed line indicates the shape of the particle unaffected by necking.

## 2.2 Wet granular matter

It is well known from everyday life that moisture can have great effect on the adhesive strength between materials, e.g. sand castles can be built from wet sand while dry sand is freely flowing and not easily mounded. Depending on the moisture content of a granular material it may be in either pendular, funicular, capillary or droplet regime as shown in Figure 2:3 (Mitarai & Nori, 2006).

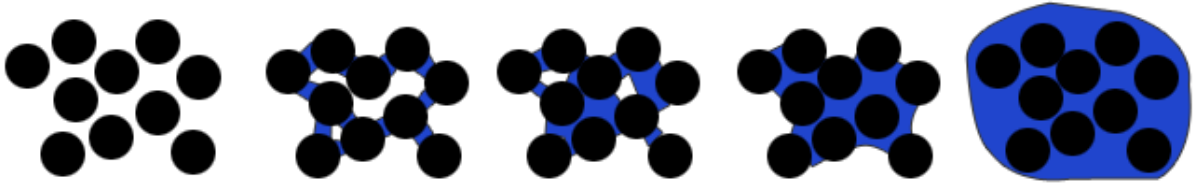


Figure 2.3. Liquid regimes in granular material from left to right: dry, pendular, funicular, capillary, droplet regime.

Each regime shows a different behaviour in terms of the capillary bridges. In the pendular state air will form a continuous phase and interstitial fluid is found as distinct liquid bridges between particle pairs. In the funicular regime, liquid bridges may coalesce, with possible interactions between more than two particles at the same time. Increasing liquid content further the capillary state is reached, in which water will form the continuous phase and no discrete bridges can be found. When the liquid content approaches saturation a suspension of particles in water is found and the state of a slurry is reached.

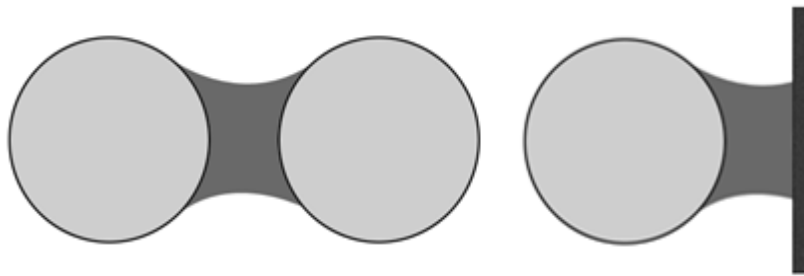


Figure 2.4. Pendular liquid bridge between two spheres and between a sphere and a wall.

### 2.2.1 Pendular liquid bridges and capillary forces

Consider a static pendular liquid bridge in thermodynamic equilibrium with the surrounding fluid between two spheres or a sphere and a wall such as shown in Figure 2.4. In such bridges, there are two different phenomena giving rise to an axial force on the bodies connected by the bridge, the Laplace pressure force and the surface tension force. The sum of these two forces gives the total static capillary force:

$$F_{cap} = F_{Wetting} + F_{Laplace} \tag{16}$$

The surface tension force, or wetting force, arise due to the surface tension of the liquid acting on the perimeter of the solid-liquid contact area. The contact angle, describing the spreading of liquid drop on a flat surface is determined by the Young equation (Butt, 2010):

$$\gamma_{solid} = \gamma_{solid-liquid} + \gamma_{liquid} \cos(\theta) \quad (17)$$

The second term in the capillary force is the Laplace pressure force, or suction pressure force. Because of the curvature of the liquid meniscus the pressure inside the bridge will not be the same as that of the surrounding fluid. If the interacting particles are small enough that gravity has negligible influence on the shape of the liquid meniscus, the pressure difference across the bridge is solely described by the Young Laplace equation (Butt, 2010):

$$\Delta P = \gamma_l \left( \frac{1}{r_1} + \frac{1}{r_2} \right) \quad (18)$$

where  $r_1$  and  $r_2$  are the principal radius of curvature of the meniscus as shown in Figure 2:5.

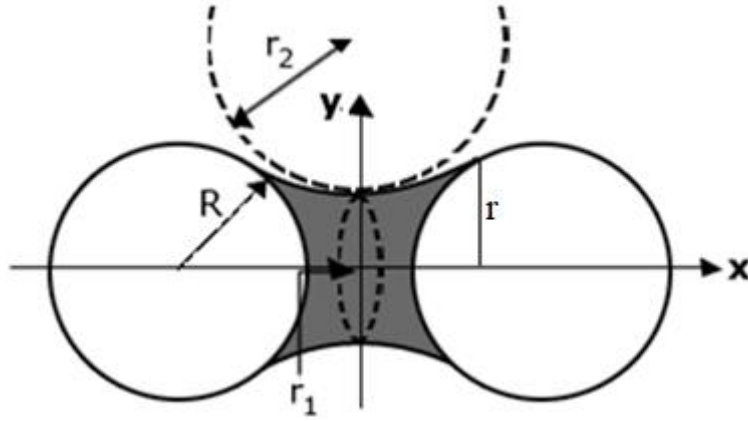


Figure 2:5. The local curvature of the pendular liquid bridge is described by the principal radius's,  $r_1$  and  $r_2$ , shown by the dashed lines.  $R$  is the particle radius,  $r$  is the radius of the bridge at the three-phase contact line and  $y(x)$  is the local bridge radius at distance  $x$  between bridge neck and three-phase contact line.

The exact form of the Young-Laplace equation, if the effect of gravity is negligible, is given by equation 19 (Lian, 1993):

$$\Delta P = \gamma_l \left( \frac{1}{r_1} + \frac{1}{r_2} \right) = \gamma_l \left( \frac{Y''}{(1+Y^2)^{\frac{3}{2}}} - \frac{1}{Y\sqrt{(1+Y'^2)}} \right) \quad (19)$$

where  $Y$  the dimensionless bridge radius  $r_2/r$ , see Figure 2:4, and prime denotes derivative with respect to the  $x$ -coordinate.

There are two distinctly different starting points in the derivation of a capillary force equation, yet in both approaches the general difficulty lies in the description of the radius of curvature of

the meniscus (Lambert and Valsamis, 2013). One approach is to express the total surface energy of the liquid bridge and derive the expression with respect to one of the parameters, such as for example the separation distance, whereby the force is obtained as a function of the parameter chosen. Any liquid bridge will have three interfaces, solid-liquid, solid-vapor and liquid-vapor and the total surface free energy of the bridge is then given by:

$$W = W_{sl} + W_{sv} + W_{lv} \quad (20)$$

The greatest difficulty lies in determining the liquid-vapor and vapor-solid interface on which the surface energy is determined (Lambert and Valsamis, 2013). The capillary force equation is then obtained by deriving the expression for the surface energy with respect to the parameter of choice, e.g. interparticle separation distance (Lambert and Valsamis, 2013)

$$F_{cap} = F_{Laplace} + F_{Wetting} = -\frac{dW}{dz} \quad (21)$$

In the other method, the shape of the meniscus is used to directly calculate the force. This approach can be divided further based on how the shape of the meniscus is determined. Firstly, for bridges in thermodynamic equilibrium the radius of curvature of the bridge is described by the Young Laplace equation. In general, no analytical solution exists for this equation and the term exact solution is referring to the numerical integration of Young-Laplace equation (de Lazer, 1999), (Lian, 1993). By introducing simplifications, it is possible to forego numerical integration of the exact solution. This is typically done by approximating the solution a priori, for example by inspecting the apparent shape of the bridge and applying it as the actual shape of the bridge when calculating the bridge radius. The most well-known is the toroidal, or circular, approximation as developed by Fisher (1926).

### 2.2.2 Capillary forces in DEM

Only solid phases are simulated in DEM and the fluid phase is explicitly disregarded. Any fluid forces acting on the particle, such as the capillary force due to pendular liquid bridges, must be modelled by parameters available in the DEM simulation. It would be possible to calculate the exact solution of the capillary force in DEM. However, the numerical integration of the Young-Laplace equation is far too costly to implement. Several approaches have been taken to incorporate capillary force models in the DEM framework without the need for numerical

integration of the exact solution. Implementation in DEM has been done through look up tables of the exact solutions calculated a priori (Shi & McCarthy, 2008) and by regression models fitted to solutions of the toroidal approximation for several particle configurations (Mikami, 1998). Another option is to implement closed form approximations that are explicit functions of available simulation parameters. Such equations were derived by Rabinovitch (2005) under the assumption of a constant volume of the liquid bridge. As opposed to the previously described equilibrium condition where the radius of the curvature of the bridge is determined by satisfying the Kelvin equation, the radius is now determined by geometrical relations with separation distance and bridge volume. The assumption of constant volume bridge is typically made for non-volatile liquids such as oil or in situations where the bridge is being pulled fast. If the pulling timescale is smaller than the characteristic timescale of evaporation and condensation, thermodynamic equilibrium is not attained and the bridge volume is approximately constant (Butt, 2010). An estimate of the characteristic time scale of evaporation is given by the following equation (Butt, 2010):

$$t_c = - \frac{R_{eff} \gamma_L}{D_{AB,air} P \ln\left(\frac{P}{P_0}\right)} \quad (22)$$

Assuming typical parameter values for the simulation conditions to be: relative humidity 0.4, temperature 25C°, diffusion coefficient  $D_{AB,air} = 2.4 * 10^{-5} [\frac{m^2}{s}]$  and surface tension  $\gamma_L = 0.073 [\frac{N}{m}]$ , the characteristic time scale is calculated to be 38 $\mu$ s. Considering the velocities at which the agglomerate impacts (0.5-5.2 m/s) it is reasonable to assume that pulling of the bridges at impact can be considered as rapid with respect to the characteristic time scale of evaporation and condensation and that equilibrium is not attained. It is therefore assumed that the liquid bridge volumes are approximately constant. The capillary force can then be modelled by closed form approximations for constant volume liquid bridges between two spheres and between a sphere and a wall as presented by Rabinovich (2005).

### 2.2.2.1 Capillary force between a sphere and a wall

(Rabinovich, 2002) derived an expression for the capillary force between an ideally smooth, solid sphere and a flat surface as shown in Figure 2:6.

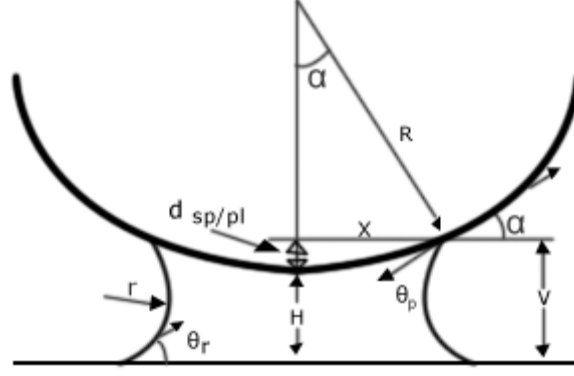


Figure 2:6. Pendular liquid bridge between a sphere and a plate.

First, the y-coordinate of the solid-liquid-vapor contact line (see Figure 2:6), can be determined by geometrical relationship through equation 23.

$$y = R + H - R\cos(\alpha) = r\cos(\theta_f + \alpha) + r\cos(\theta_p) \quad (23)$$

In equation 23, R is the particle radius, H is the separation distance,  $\alpha$  is the half-filling angle, r is the lesser radius of meniscus and  $\theta_f, \theta_p$  are the contact angle of the particle and the flat respectively. Moreover, assuming the bridge volume is small enough such that  $x, y$ , and  $r \ll R$ , the half-filling angle,  $\alpha$ , can be solved for:

$$\alpha = -\frac{r\sin(\theta_f)}{R} + \sqrt{\frac{r^2\sin^2(\theta_f)}{R^2} - \frac{2H-2r(\cos(\theta_f+\theta_p))}{R}} \quad (24)$$

If the contact angles are small,  $\theta_f, \theta_p \ll 1 \text{ rad}$ , equation 24 can be further simplified as:

$$\alpha^2 = \frac{2H-2r(\cos(\theta_f+\theta_p))}{R} \quad (25)$$

The Laplace pressure force is determined as:

$$F_{Laplace} = \pi x^2 \Delta P \quad (26)$$

Assuming the lateral radius to be much greater than the lesser radius Young-Laplace equation is simplified as:

$$\Delta P = \gamma_l \left( \frac{1}{r_1} + \frac{1}{r_2} \right) = \gamma_l \left( \frac{1}{r} - \frac{1}{x} \right) = \frac{\gamma_l}{r} \quad (27)$$

Substituting equation 27 in to 26, the Laplace pressure force is given by:

$$F_{Laplace} = \frac{\pi x^2 \gamma_l}{r} \quad (28)$$

The lateral radius of the bridge is determined by geometrical relation through equation 29:

$$x = R\alpha \quad (29)$$

Giving:

$$F_{laplace} = \frac{\pi \gamma_l R^2 \alpha^2}{r} \quad (30)$$

Substitute equation 25 for the half-filling angle in to equation 30:

$$F_{sppl} = -4\gamma_l \pi R \cos(\theta_{eff}) \left(1 - \frac{H}{2r \cos(\theta_{eff})}\right) \quad (31)$$

In equation 31,  $\theta_{eff}$  is the effective contact angle ( $\theta_{eff} = (\theta_f + \theta_p)/2$ ). For small liquid volumes and contact angles the half filling angle is typically small and the following approximation is introduced,  $(d_{sppl} + H) \approx 2r \cos(\theta_{eff})$ , in which case equation 31 can be written as equation 32 (Israelachvili, 2011):

$$F_{sppl} = -\frac{4\pi R \gamma_l \cos(\theta_{eff})}{\left(1 + \frac{H}{d_{sppl}}\right)} \quad (32)$$

Rabinovitch (2005) arrives at the final equation for the capillary force by including an expression for the wetting force:

$$F_{sppl} = -\frac{4\pi R \gamma_l \cos(\theta_{eff})}{1 + \frac{H}{d_{sppl}}} - 2\pi R \gamma_l \sin(\alpha) \sin(\theta_{eff} + \alpha) \quad (33)$$

The immersion height,  $d_{sppl}$ , is calculated from geometrical relationship between the constant bridge volume and separation distance (Rabinovich, 2005):

$$d_{sppl}(H, V) = -H + \sqrt{H^2 + \frac{V}{\pi R}} \quad (34)$$

In equation 34 the separation distance, H, and bridge volume are known input variables while the half-filling angle is an unknown parameter. As it is not a material property it is not known a-priori and must be determined in the calculation of the capillary force. During the derivation of the capillary force equation 25 was used for the half-filling angle. However, equation 25 is

describing the half-filling angle in a liquid bridge in thermodynamic equilibrium such that the radius,  $r$ , is determined by the Kelvin equation. It is therefore not applicable for calculating the force in equation 33. For a non-equilibrium liquid bridge between a wall and a sphere Rabinovich (2005) presents the following relationship between half-filling angle, bridge volume and separation distance:

$$\alpha_{spsp}^2 = \frac{2H}{R} \left( -1 + \sqrt{\left(1 + \frac{2V}{\pi R H^2}\right)} \right) \quad (35)$$

### 2.2.2.2 Capillary force between two spheres

The equation for a liquid bridge between two spheres as presented by Rabinovich (2005) is based on the derivation by Israelachvili (1992). For two particles with radius  $R$  and contact angle  $\theta$  Israelachvili (1992) derived an equation for the total energy of the liquid bridge in thermodynamic equilibrium:

$$W_{tot,sppl} = -2\pi\gamma_l R^2 \alpha^2 \cos(\theta_{eff}) \quad (36)$$

In this expression, the solid-vapor and the vapor-liquid surfaces were neglected and only the energy of the solid-liquid surface of the bridge is taken into account. Deriving the expression for the surface free energy,  $W_{tot,sppl}$ , with respect to the separation distance,  $H$ , between the spheres an equation for the capillary force is obtained:

$$F_{spsp}(H, V) = -\frac{dW_{tot,sppl}}{dH} = 2\pi R^2 \alpha \gamma_l \cos(\theta_{eff}) \frac{d\alpha}{dH} \quad (37)$$

where  $V$  is the liquid bridge volume. For small half-filling angles,  $\alpha$ , the bridge volume is given by:

$$V_{spsp} = \pi R^2 \alpha^2 H + 0.5\pi R^3 \alpha^4 \quad (38)$$

Since the volume is constant:

$$\frac{dV_{spsp}}{dH} = 0 \quad (39)$$

An expression for the unknown derivative in equation 37 is obtained by solving equation 38 for  $\alpha$  and taking the derivative with respect to  $H$ :

$$\frac{d\alpha}{dH} = -\frac{1}{\left(\frac{2H}{\alpha}\right) + 2R\alpha} \quad (40)$$

The expression for the Laplace Pressure force is obtained by introducing a new parameter called the immersion height,  $d_{spsp}$ , which is a function of the bridge volume and the separation distance. As seen in Figure 2:5 the immersion height is the distance between the three-phase contact line and the particle radius. This parameter is introduced following the substitution of equation 40 in to equation 37:

$$F_{spsp}(H, V) = -\frac{2\pi R\gamma_l \cos(\theta_{eff})}{1 + \left(\frac{H}{2d_{spsp}(H, V)}\right)} \quad (41)$$

An expression for the immersion height,  $d_{spsp}$ , is found by geometrical relationship between the constant bridge volume and separation distance through rearrangement of equation 38 (Rabinovich, 2005):

$$d_{spsp}(H, V) = \left(\frac{H}{2}\right) \left(-1 + \sqrt{\left(1 + \frac{2V}{\pi R H^2}\right)}\right) \quad (42)$$

To obtain an expression for the full capillary force Rabinovitch (2005) adds a term for the axial component of the wetting force and equation 43 is obtained:

$$F_{spsp}(H, V) = -\frac{2\pi R\gamma_l \cos(\theta_{eff})}{1 + \left(\frac{H}{2d_{spsp}(H, V)}\right)} - 2\pi R\gamma_l \sin(\alpha) \sin(\theta_{eff} + \alpha) \quad (43)$$

In equation 43 the separation distance, H, and bridge volume are known input variables while the half-filling angle is unknown. In the case of a non-equilibrium liquid bridge between two spheres Rabinovich (2005) presents the following relationship between half-filling angle, bridge volume and separation distance:

$$\alpha_{spsp}^2 = \frac{H}{R} \left(-1 + \sqrt{\left(1 + \frac{2V}{\pi R H^2}\right)}\right) \quad (44)$$

### 2.2.2.3 Extending to polydisperse systems

Rabinovitch investigated the use of the derived formulations of the capillary force between equal spheres for the interaction between uneven spheres using the harmonic mean:

$$R = R_{eff} = 2 \frac{R_1 R_2}{R_1 + R_2} \quad (45)$$

The validity of the derived equations is confirmed through comparing with experimental results of the liquid bridge of an oil droplet between to uneven silica spheres with size ratios of 1.84, 1.71 1.44. However, the validity of the equation for larger size ratios is not discussed.

#### 2.2.2.4 Limits of applicability

Looking closer at the derived equations for the capillary force, it is found that neither is dependent on the liquid bridge volume at zero separation distance. In the extreme case, these expressions would assign a capillary force even though the relative humidity or the liquid content is zero. (Rabinovich, 2002) discussed the limit of applicability stating that the equation must be bound by a lower limit of the liquid bridge volume. This lower limit could be identified by the smallest amount of liquid that is able to form a liquid meniscus or below which the continuum description of the liquid bridge breaks down (Rabinovich, 2002). Fisher and Israelachvili (1981) measured the adhesion of mica surface in water vapor, it is found that equation 46 is valid when bridge radii exceed approximately 5 nm.

$$F = 4\pi R \gamma_l \cos(\theta_{eff}) \quad (46)$$

This equation corresponds to the maximal capillary force that is exerted at contact between two interacting surfaces as derived from equation 43.

An upper limit of applicability is not discussed. However, as the described equations are derived explicitly for pendular bridges, the upper limit should be determined by the liquid content necessary for transition to the funicular regime.

#### 2.2.3 Liquid bridge formation distance

A liquid bridge is formed when the liquid on two surfaces first come in to contact. In this study, it is assumed that the water on each particle is homogeneously spread out over the surface. The addition of liquid on the surface of a particle thus give rise to an effective radius at which the particles water will come in to contact with another surface. The formation distance,  $\delta_f$ , is the difference between effective radius and the particle radius. This effective radius of the particle can be determined from the following expression:

$$V_{r+\delta} - V_p = V_l \quad (47)$$

where  $V_{r+\delta}$  is the volume of a particle with the effective particle radius  $(r + \delta_f)$ ,  $V_p$  is the particle volume and  $V_l$  is the volume of liquid on the particle surface. The surface liquid volume is given in percent of particle volume:

$$V_l = \alpha_{slc} * V_p \quad (48)$$

where  $\alpha_{slc}$  is the surface liquid content in percent of particle volume. The formation distance can be solved for through:

$$\alpha_s r^3 \frac{4\pi}{3} = \left( (r + \delta_f)^3 - r^3 \right) \frac{4\pi}{3} \quad (49)$$

$$\alpha_s r^3 - 3r^2 \delta_f - 3r \delta_f^2 - \delta_f^3 = 0 \quad (50)$$

The formation distance for a particle pair is given by the sum of the cut-off radii, calculated extreme values can be found in Appendix A.1. The greatest formation distance between any two pair of particles is 1.66 % of the smaller particles radius, it is found for particles with 1% liquid content between the largest (44 $\mu$ m) and the smallest (11 $\mu$ m) particle. During the formation of the bridge the liquid contribution from each particle is based on an average coordination number of the agglomerate. In a primitive cubic packing of even spheres the average coordination number is six (Hoppe, 1970). Assuming all surface liquid to be distributed evenly between the bridges, each bridge receives one sixth of the particle's surface liquid content.

## 2.2.4 Liquid bridge rupture distance

The liquid bridge between to moving spheres with a constant volume bridge will elongate and become thinner with increasing separation distance until a certain point where it becomes unstable and ruptured. Lian (1993) theoretically investigated the stability of a constant volume bridge between two even sized spheres with different contact angles. The separation distance was determined by first specifying one of the output parameters, such as for example the half-filling angle or neck diameter, and then solving the exact solution of the capillary force which gives a value for the separation distance. The chosen parameter value was then varied and the corresponding solution was obtained. By plotting the parameter values and the corresponding

separation distances, a maximal value of the separation distance is found which, is taken as the critical rupture distance. More calculations of the rupture distance were done by determining the separation distance as a function of the minimum surface energy of the bridge. The values of the rupture distance from both techniques coincide and a simple relationship between the dimensionless rupture distance and the liquid bridge volume is identified:

$$2H_c^* = (1 + 0.5\theta_{eff})\sqrt[3]{V^*} \quad (51)$$

where  $\theta_{eff}$  is the effective contact angle,  $H_c^*$  is the scaled critical rupture distance and  $V^*$  is the scaled liquid bridge volume defined as:

$$H_c^* = \frac{H_c}{R_{eff}} ; V^* = \frac{V_{lb}}{R_{eff}^3} ; R_{eff} = 2 \left( \frac{R_1 R_2}{R_1 + R_2} \right)$$

The critical rupture distance between even and uneven sized spheres and between a sphere and a flat surface was investigated experimentally by Willet (2000). The rupture distances calculated by the expression presented by Lian (1993) is compared to the experimental results and it is found to overestimate the critical rupture distance between a sphere and a flat surface. By fitting to the experimental results, Willet presents new expressions for the critical rupture distance. In the case of two uneven spheres, or a sphere and a flat surface in which, the size ratio  $R_2/R_1 > 0$ , the following expression is suitable:

$$2H_c^* = \left( 1 + \frac{\theta}{4} \left( \frac{R_2}{R_1} + 1 \right) \right) \left( V^{*\frac{1}{3}} + \left( \frac{R_2}{2R_1} - \frac{2}{5} \right) V^{*\frac{2}{3}} \right) \quad (52)$$

For two even spheres equation 52 is found to underestimate the rupture distance and Willet (2001) suggests the following expression, fitted to even sphere experiments:

$$2H_c^* = \left( 1 + \frac{\theta}{2} \right) \left( V^{*\frac{1}{3}} + 0.1V^{*\frac{2}{3}} \right) \quad (53)$$

## 2.2.5 Liquid distribution at rupture

In the process of rupture of a liquid bridge, the liquid will be redistributed between the two interacting bodies. Based on the assumption that rupture occurs at the thinnest point of the bridge and that each sphere retains the amount of liquid that is left on its side of the rupture point, Shi & McCarthy (2008) calculated the redistribution between even and uneven spheres

with different contact angle configurations. The liquid volume on each side of the rupture point is calculated by applying the parabolic approximation and determining the shape of the liquid bridge at the time of rupture. It is found that for monodisperse spheres with zero contact angle, the liquid is equally distributed to both spheres. For a size ratio of 1.25 and zero contact angle the distribution is approximately 60-40.

## 2.2.6 Dynamic liquid bridge forces

The previously derived equations for the capillary force, only considered the static forces of a liquid bridge between two particles. In the case of impacting agglomerates, the situation will be dynamic and liquid bridges will be pulled and elongated or pushed and compressed by the relative movements of the particles. In this situation, an additional dynamic force will be exerted by the bridge due to the viscous resistance to the motion of the fluid. Theoretically this can be explained by the lubrication theory, in which Newton's equation for thin films relates the pressure in the film to the separation distance between the particle surfaces (Pitois, 2000):

$$\frac{d}{dr} \left[ rH^3 \frac{dP}{dr} \right] = 12\mu r \frac{dD}{dt} \quad (54)$$

where  $H$  is the separation distance between the two contacting surfaces covered by the liquid bridge,  $P$  is the pressure liquid pressure,  $r$  is the radius of the contact area and  $\eta$  is the fluid viscosity. In the case of two rigid particles, the following equation was derived for the axial direction of the viscous force (Nase, 2001):

$$F_{visc,n} = 6\pi\mu R_{eff} v_n \frac{R_{eff}}{H} \quad (55)$$

The tangential component of the viscous force can be determined by (Nase, 2001):

$$F_{visc,t} = \left( \frac{8}{15} \ln \left( \frac{R_{eff}}{H} \right) + 0.9588 \right) 6\pi\eta R_{eff} v_t \quad (56)$$

where  $v_t$  is the relative tangential velocity. For small separation distances, these expressions for tangential and normal viscous forces tend to infinity. In reality, particles will experience a minimum, finite separation distance because of surface asperities (Nase, 2001).

### **3. Methodology**

This chapter begins with findings from the literature study of material properties. The DEM model and implementation of capillary forces will thereafter be treated along with the formation procedure and characterization of wet and dry agglomerates. In the end of the chapter post processing methods of simulation data will be presented.

#### **3.1 Material properties**

In physical testing of dust contamination in the car industry it is common to use Arizona test dust, ATD, as a model compound (Farin Daryosh (Volvo Car Corporation), Personal Communication). The target system of wet road dust agglomerates is therefore modelled as ATD. The wall impact surface could be any of the surface materials on the car exterior and in this study the wall is specified as a glass surface.

##### **3.1.1 Elastic mechanical properties**

Reagle (2013) measured the coefficient of restitution for oblique impacts of ATD particles with nominal size 20-40  $\mu\text{m}$  on to a stainless-steel surface at 27 m/s. The impact angle was varied between 30°-80° and measured mean COR ranged from 0.9 to 0.4. Extrapolating the results, following the declining trend towards normal impact, a value of 0.3 for particle-wall collision is specified. Weir & Tallon (2005) investigated the relationship of COR between low-velocity normal impacts for sphere-sphere and sphere-plate for elastic-plastic particles. Experiments show that for identical, even sized spheres, the COR for sphere-sphere collisions is about 19 % smaller than for the sphere-plate collision. The value of particle-particle COR is therefore set to 0.25.

The elastic modulus and Poisson's ratio of the dust particles is approximated by the value of soil found in the literature 2.86 GPa (Yang, 2014). Values for the Poisson's ratio, coefficient of friction and coefficient of rolling friction is approximated by that of polystyrene filled glass beads (Khalilitehrani, 2016)

Wall material properties of Poisson's ratio coefficient of restitution, particle-wall friction and particle-wall rolling friction are approximated by polystyrene filled glass beads (Khalilitehrani,

2016) and the Young's modulus of soda-lime glass (Oliver & Pharr, 1992), Interface energies was obtained for “dust” particles (0.09995 J/m<sup>2</sup>) and quartz (0.0803) (Jordan, 1954).

The particle-wall interface energy is calculated through combining relations given by Israelachvili (2011). The Hamaker constant for two similar materials can be used to calculate the Hamaker constant for interaction between two dissimilar materials through a third material through a combining relation. The third media in these simulations is air for which the interface energy is approximately zero and the Hamaker constant can be calculated as follows (Israelachvili, 2011):

$$A_{132} = \sqrt{A_{11} * A_{22}} \quad (57)$$

Or equivalently for the interface energy

$$W_{132} = \sqrt{W_{11} * W_{22}} \quad (58)$$

### 3.1.2 Capillary force properties

Particle and wall properties are approximated as glass when determining their contact angles. The contact angle for water on untreated glass was found to be 4.5-6.7 degrees due to contact angle hysteresis (Wei, 1993) and a value of 5 degrees is specified in the simulation properties. Water-air surface tension is set to 73 mN/m (Israelachvili, 2011). The dynamic capillary force is dependent on the viscous property of the liquid which is set to the value of water at 20°, as 100 mPas (Mörtstedt, 2012).

Table 3:1 Material properties used in simulations. (refer to reference by numbers in the table)

Property	Particles	Wall
Young's Modulus [GPa]	0.3	70
Poisson's Ratio [-]	0.3	0.3
Density [ $\frac{\text{kg}}{\text{m}^3}$ ]	2500	*
Normal Coefficient of Restitution, Particle-Particle [-]	0.25	*
Normal Coefficient of Restitution, Particle-Wall [-]	0.3	0.3
Interface Energy [J/m <sup>2</sup> ]	0.09995	0.0803
Coefficient of friction, Particle-Particle [-]	0.17	*
Coefficient of friction, Particle-Wall [-]	0.35	0.35
Coefficient of rolling friction, Particle-Wall [-]	0.02	0.02
Contact angle [°]	5	5

\* Parameter not used in simulations

### 3.1.3 Particle size distribution

The size distribution for the polydisperse agglomerate is based on the size distribution of the ISO 12103-1, A2 Fine test dust (Powder Technology INC, 2016) shown in Figure 3:1.

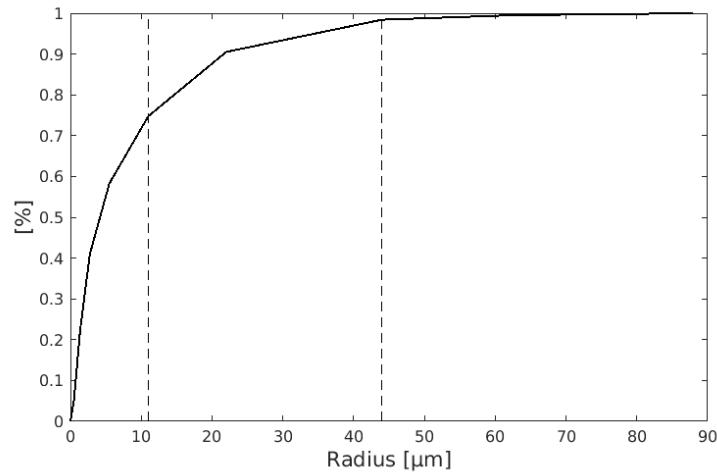


Figure 3:1. Plot of the cumulative mass distribution for fine Arizona test dust. Dashed lines indicate the size range within which the simulated agglomerate is based on.

However, as the radius ranges between  $2.25 \mu\text{m}$ - $88 \mu\text{m}$  the number of fine particles will be too great if the full distribution is to be included. The distribution is therefore cut between  $11 \mu\text{m}$ - $44 \mu\text{m}$  as is shown by the dashed lines in Figure 3:1. This size range corresponds to 25 % of the total mass distribution. To determine the number of particles with each radius, the chosen size range is further split up in to smaller ranges according to

Table 3:3. Each size range is then approximated as uniformly distributed, see Figure 3:2, and particles assigned radii accordingly.

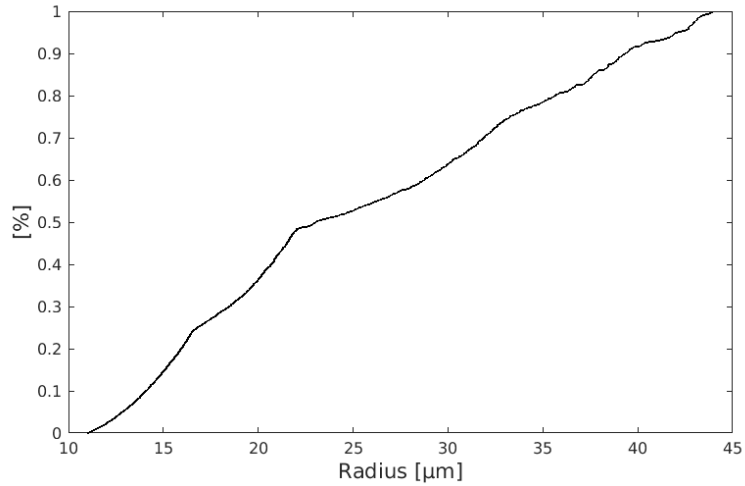


Figure 3-2: Cumulative mass distribution of the polydisperse agglomerates

To further reduce computational burden, the relative weight distribution of each size range is shifted towards larger sizes compared to ATD, see table 3.2 and 3.3.

Table 3-2 Mass distribution of the size ranges in ATD.

Radius [ $\mu\text{m}$ ]	Cumulative Mass Probability [%]	Mass Probability [%]	Relative mass probability [%]
11–22	90.5	15.75	66
22–44	98.4	7.9	33

Table 3-3: Cumulative mass distribution, mass based probability and number of particles for the polydisperse agglomerates. In the utmost right column, the number of particles had the original relative weight been used is shown.

Radius [ $\mu\text{m}$ ]	Cumulative mass probability %	Range probability %	Particles	Particles (without relative weight shifted)
11–16.5	24	24	2566	3573
16.5–22	48	24	953	1328
22–33	74	26	346	220
33–38.5	87	13	82	51
38.5–44	100	13	53	33

## 3.2 Agglomerate liquid content

In this thesis, the dry and semidry state is to be investigated and the liquid contents are chosen to range from 0.01% to 1%. The lowest value of 0.01% is chosen to investigate the difference in the behaviour of the agglomerate in dry state and a liquid volume close to the lowest onset of the capillary forces. This is approaching the minimum liquid necessary for a liquid bridge formation as discussed in the theory section on capillary forces. The upper value is chosen as 1%, such that the effect of the liquid content be investigated while keeping well out of the range of the funicular regime.

## 3.3 DEM implementation

Simulation of agglomerate impacts are performed with the open-source software LIGGGHTS that is built for DEM modelling. The standard source code in LIGGGHTS comes with some contact models for both wet and dry contacts. It is also possible to modify the source code to implement new contact theories or physics.

### 3.3.1 Contact force modelling

Contact forces are only calculated between particles when an overlap exists. The total force acting on a body is composed by normal and tangential forces, which is composed of an elastic and a viscous dampening part:

$$F = (Fne - Fnd) + (Fte - Ftd)$$

Depending on which contact model is used, the force is calculated by either Hertz or JKR theory of contact mechanics as described in the theory section.

#### 3.3.1.1 Dry particle-particle/wall contact forces

Because of the adhesive nature of sand particles in the target agglomerate system the JKR theory is supposedly the most appropriate model for the contact force. The applicability of the JKR theory can be determined by the Tabor number. In these calculations the equilibrium separation distance,  $z_o$ , is set to  $1.65\text{\AA}$  as it is considered as approximately universal value (Israelachvili, 2011). Calculated extreme values for particle-wall and particle-particle interactions are shown below:

$$\left( \frac{R W^2}{E_{eff}^2 D_o^3} \right)^{\frac{1}{3}} \rightarrow 60 \text{ (particle – wall) } 65 \text{ (particle – particle)}$$

As the values are well above the lower value of applicability of the JKR theory (3.0), the contact forces will be calculated by the implementation of JKR theory as performed by Nguyen et al (2014). Van der Waals forces are generally very short range and in this implementation by Nguyen (2014) calculations are simplified by the assumption that contacts are broken once a finite separation distance is achieved.

### 3.3.1.2 Wet particle-particle/wall contact forces

It is found that the Hamaker constant of silica interacting through water is 8 times smaller than that of interaction through air (Rabinovich, 2002). The adhesion due to van der Waals forces is therefore assumed negligible and contacts are modelled by Hertz theory.

### 3.3.2 Capillary force modelling

The LIGGGHT's software comes with two built in capillary force models. One of these is based on the work by Rabinovich (2005), (Lian, 1993) and Nase & McCarthy (2001). However, this standard model as it comes with the software is not correctly implemented for application in this thesis. The source code only contains a particle-particle force equation, it assumes that rupture and formation distance is equal and described by the rupture distance as derived by Lian (1993), i.e. equation 51. Thus, in this work, a revised capillary model is implemented with equations according to the theory of pendular liquid bridges as described in the theory section. The following section summarize the implemented theory and equations.

#### 3.3.2.1 Capillary force equations

Depending on whether the two bodies connected by a liquid bridge are in contact or not there are two different equations to calculate the capillary force. In the case that the bodies are not in contact but the liquid bridge is still stable, there is a ranged capillary force acting on the bodies. For the ranged capillary force between two spheres the force is calculated through equation 43. This equation is solved explicitly for the two input variables, liquid bridge volume and particle separation distance, after substitution of equation 42 and 44 for the immersion height and half-filling angle. The ranged capillary force between a sphere and a wall is calculated through

equation 33 after substitution of equation 34 and 35 for the half-filling angle and immersion height. In the case of contact between the bodies, at zero separation distance or deformation, the capillary force exerted by liquid bridges in the pendular regime is maximal and independent on liquid volume. The capillary force between two bodies in contact is assumed to be independent on the size of the overlap and is capped at the maximal value as calculated through equation 59 and 60:

$$F_{sppl} = -4\pi R\gamma_l \cos(\theta_{eff}) \quad (59)$$

$$F_{spsp} = -2\pi R_{eff}\gamma_l \cos(\theta_{eff}) \quad (60)$$

### **Formation distance**

Because of the small formation distances, see calculated values in appendix A.1. It is approximated that the formation occurs at the first moment of contact between two particles or between a particle and the wall.

### **Liquid contribution to the bridge**

Assuming the agglomerate is forming primitive cubic packing, the average coordination number is six (Hoppe, 1970). Each bridge should then contain 16 % of the particles surface liquid volume and it is assumed that in any bridge formation 16 % of the surface liquid volume goes in to the bridge formation.

### **Rupture distance**

Capillary forces are active as long a liquid bridge exists between to surfaces. Liquid bridges are assumed to be stable until the particle separation distance is greater than specified by equation 52 for sphere-wall and equation 53 for sphere-sphere interaction. At greater separation distance forces are zero as the bridge ruptures and liquid is redistributed between particles.

### **Liquid distribution at rupture**

When a liquid bridge is ruptured it is assumed that the liquid in the bridge is divided between the particles in the same proportion as it was formed and each particle is regaining as much liquid as it contributed in the formation. The model is simplified by assuming that each particle retains the same amount of water it contributed to the bridge.

### Minimum separation distance for the viscous force

The minimum separation distance is specified as a ratio of the effective radius. A minimum value from this equation is not only a matter of physical reasoning, the numerical stability of the simulation is affected when the equation tends to infinity. Therefore, at first glance it appears that the chosen value of this minimum distance could significantly affect the magnitude of the capillary force and the simulation result. The parameter should be considered a material property reflecting the surface roughness of the particles. Nase (2001) assumed a value of  $10^{-6}$  for calculating the force of glass particles in the size of 0.5-10 mm, corresponding to 0.2% of the smallest particle diameter. Lian (1998) made a sensitivity analysis of the parameter for simulation of impact between two agglomerates and findings suggests the value does not have significant effect on the simulation given that it is small enough. A value 0.1% of the effective radius is deemed appropriate for the minimum distance.

### 3.3.3 Simulation time step

Cundall and Strack (1978) states that the for the approximation of deformation as an overlap to be valid, the size of the overlap must be negligible compared to that of the particles size. Moreover, because of the explicit integration schemes, correct size of the simulation time step is critical for numerical stability and accuracy of DEM simulations (Li, 2011). Should the time step be too large it can cause too great overlap increase between each iteration, resulting in unphysically high repulsive force and increase of kinetic energy. Adhesive forces have approximately the same characteristic time scale as the Hertz elastic response time. It is thus necessary to have time steps a fraction smaller than this value to fully resolve the contact duration (Li, 2011). To determine the necessary timestep, several characteristic time scale estimates were calculated and compared. In a polydisperse system the timestep is specified by the smallest time scale in the system and the following calculations is therefore based on the smallest particles for particle-particle and particle-wall interaction. The time step value is set to 1% of the calculated time scale. The elastic response time for Hertz contact theory can be calculated through equation 61 (Marshall & Li, 2014)

$$t_c = 2.868 \left( \frac{m_{eff}^2}{E_{eff}^2 R_{eff} v_{max}} \right)^{\frac{1}{5}} \quad (61)$$

$$\Delta t = \min[\textit{Particle} - \textit{Wall} (3.75 \text{ ns}) ; \textit{Particle} - \textit{Particle} (5.67 \text{ ns})]$$

For simulation using Hertz contact mechanics it is generally acknowledged from empirical simulation experience that the time step should be set to one order of magnitude smaller or less than the natural oscillation period of a mass-spring system, see equation 62 (Crowe, 2011). The required timesteps for this time scale is calculated through equation 62:

$$t_c = 2\pi \sqrt{\frac{m_{eff}}{\sqrt{\frac{2R_{eff} E_{eff}}{3(1-\nu^2)}}}} \quad (62)$$

$$\Delta t = \min [\textit{Particle} - \textit{Wall} (0.34 \text{ ns}) ; \textit{Particle} - \textit{Particle} (0.57 \text{ ns})]$$

The simulation time step is set to 0.1ns, corresponding to the lower value of the calculated characteristic time scales.

### 3.3.4 Agglomerate formation

A dry polydisperse agglomerate is formed by the random insertion of 4000 particles, with size distribution according to , in a spherical region. Each size range is identified as one type of particles in the simulation. To each type, a centripetal force with magnitude 10 times the weight averaged gravitational force of each size range is applied. Particle properties are specified according to Table 3:1 and the JKR contact force model implemented by Nguyen et al (2014) is used. The simulation is run until particles velocities tend to zero and equilibrium is obtained.

Wet agglomerates are formed by changing the contact force model from JKR to Hertz and turning on the capillary force model. The simulation is restarted from equilibrated dry, agglomerate simulation, and is run until equilibrium is achieved. This procedure is done for each simulation condition, yielding three polydisperse agglomerates with liquid contents of 0.01%, 0.1% and 1%.

### 3.3.5 Characterisation

The structure and macroscopic properties of the agglomerate can be different depending on how the agglomerate is formed. It can influence the impact behaviour of the agglomerate and it is therefore important to characterize the initial agglomerate such that it can be related to regarding the post impact behaviour. Properties of the initial agglomerates are presented in table 3:4 and the final wet agglomerate with liquid content 0.01% is shown in Figure 3:3.

Table 3:4 All polydisperse agglomerates have the same property values that are shown in this table.

Agglomerate property	Value
Porosity [%]	52
Mass [mg]	0.302
Number of particles	4000
Particle radius [ $\mu\text{m}$ ]	11 – 43.94

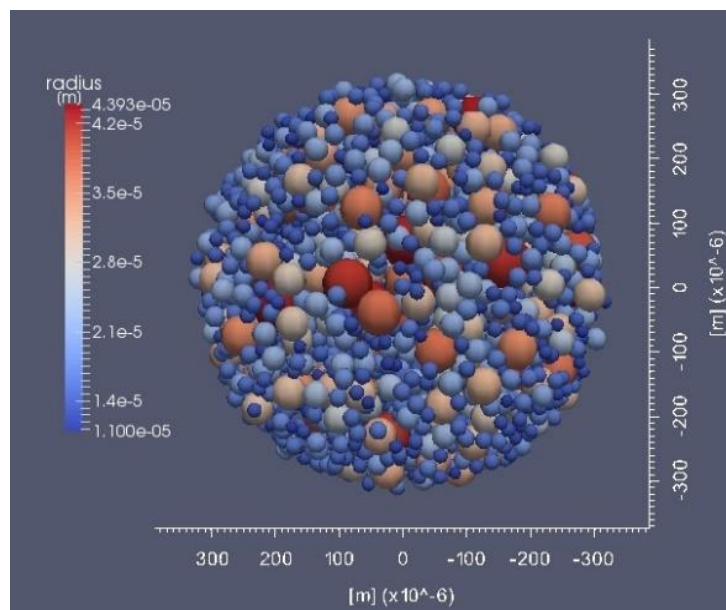


Figure 3:3. Wet, polydisperse agglomerate particles coloured according to radii. View is normal to the impact plane, impacting out from the view plane.

The coordination number distribution is found to be equal for all wet agglomerates and is shown in Figure 3:4.

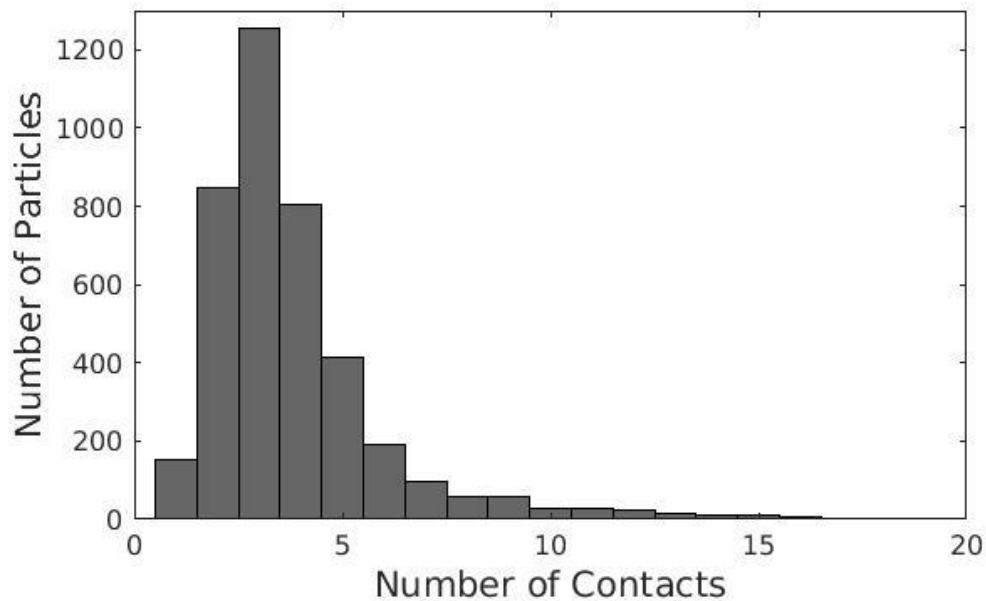


Figure 3:4. Coordination number for the polydisperse agglomerates

### 3.4 Wall normal impact procedure

A three-dimensional simulation box is created and a wall is created with material properties as given in Table 3:1. A MATLAB script is written to place agglomerates one hundred thousand time steps from the wall for each impact velocity. Impact velocities are chosen as found appropriate to allow for the possibility of observing different impact behaviors. Simulations are run until parameter values reach asymptotic values of capture ratio and damage ratio. Dump files containing simulation output information is produced every hundred thousand time steps. For simulation of dry agglomerates, the contact forces will be calculated using the LIGGGHTs implementation of JKR as created by Nguyen et al (2014). For the wet agglomerates, the built in Hertz contact mechanics model in LIGGGHTs is used along with the revised capillary force model as described in section 2.2.

## 3.5 Post processing

Text files containing information on various parameters such as particle positions, forces, velocities and overlap are extracted during the simulation. Post processing of the data are required. The post-processing procedures used to analyze the results are described in this section.

### 3.5.1 Damage ratio

From the first moment of impact a repulsive force will be exerted between the wall and the agglomerate particles in touch with the wall. The force will spread further in to the agglomerate by pairwise interaction between particles. The transmitted repulsion may be greater than the attractive force between any two particles, in which case the bond between them will break. The extent of internal damage done to the agglomerate can be measured by the damage ratio (Thornton, 1999):

$$\text{Damage ratio} = \frac{N_0 - N}{N_0} \quad (63)$$

where  $N_0$  is the initial number of bonds and  $N$  is the number of bonds at the given time step.

### 3.5.2 Initial bonds broken

Damage ratio only convey information on the ratio of broken bonds to the number of formed bonds. A negative value merely implies that the total number of bonds has increased compared to the initial state, it does not specifically state if any bonds have been broken or not. To further distinguish the behaviour a ratio measured by the absolute number of bonds broken is introduced. The ID's of the pairwise contacts in the initial agglomerates is identified and compared to the contacts at any given moment, the number of initial bonds broken is then calculated by this information. The initial bonds broken ratio is given by:

$$\text{Initial bonds broken} = \frac{N_{ID,0} - N_{ID}}{N_{ID,0}} \quad (64)$$

where  $N_{ID,0}$  is the number of initial contacts and  $N_{ID}$  is the number of initial contacts that are still active at the given time step.

### 3.5.3 Wall adhesion

An important factor of the agglomerate impact when developing effective surface cleaning systems is how many particles that adheres to the wall, and how great force that is necessary to remove them. Two measures are used to characterize the wall adhesion behaviour, the capture ratio and total adhesive force.

### 3.5.4 Capture ratio

The impact behaviour of the agglomerate will affect how many particles are ending up adhering to the wall after impact. The extent to which the agglomerate is sticking to the wall is described by the capture ratio, defined as the ratio of the number of particles adhering to the wall over the total number of particles in the agglomerate as given by:

$$\text{Capture ratio} = \frac{N_0 - N}{N_0} \quad (65)$$

### 3.5.5 Total adhesive force

Capture ratio alone does not tell the full story about the agglomerate adhesion because the force is different between wet and dry particles. Each contact is assumed to be independent, meaning that if there are more particles adhered to either of the particles for which the interaction force is calculated they do not alter the interaction force. The total force on any particle is then the sum of contact forces between immediate neighbors to this particle (Cundall and Strack 1978). The adhesive force between dry particles and the wall is calculated according to the JKR contact theory in which the maximum tensile force needed to break a contact is determined by the pull-off force, see equation 66, (Thornton, 2015):

$$F_{PO} = -\frac{3}{2}\pi R_{eff}W \quad (66)$$

In the case of wet particles, considering static mechanical equilibrium, the adhesive force is given by equation 59 which corresponds to the maximum capillary force between a sphere and a wall (Rabinovich, 2005).

### 3.5.6 Fragmentation

With increasing impact velocity, particles experience greater repulsive forces, which may cause the particles to lose contact and break loose from the agglomerate. Depending on the microscopic structure and cohesive forces between particles, they can break loose both in the groups of several particles together, i.e. fragments, or as single particles. The number of fragmented particles at certain impact velocity is a measure of the agglomerate interparticle strength. Both the number of fragments and the size of each fragment, i.e. the number of particles, will be determined using a MATLAB code of “Density-Based Algorithm for Discovering Clusters, DBSCAN. Input to DBSCAN is the position of the particles along with a neighbor radius and minimum number of particles that is considered a fragment (Ester, 1996). The neighbor radius specifies the maximum distance between two points above which the particles are not considered to be neighbors and thus not included in the same fragment. Should three or more particles be link to each other through their respective neighbor radii they are considered a fragment, see for example particle N in Figure 3:5. In this figure circles represent the respective neighbor distance for particles B to E. All particles except N is forming a single fragment with size 5. The particle labeled A is on the edge of the fragment as it is only connected to one other particle, B, which is in the core of the fragment as it is connected to two other particles, E and A. These three particles would be considered a single fragment as three particles is the minimum number of particles required. But as particles C, E and D are connected to each other they are forming a fragment with 5 particles. Particle N is not enclosed by the neighbor radius of any other particle and it is therefore not a part of the fragment.

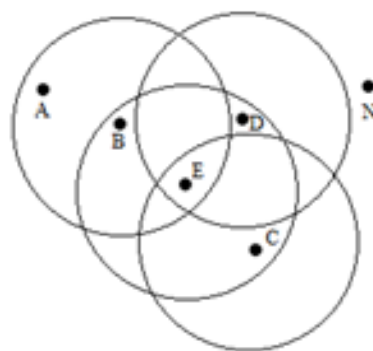


Figure 3:5. Schematic drawings of fragment determination in DBSCAN. Solid lines indicate cut-off radius from the particles center.

Application of DBSCAN on polydisperse systems may result in spurious detection of fragments. Because only one neighbor radius is specified for the system it is equal for all particles and independent on their radii. This can result in overestimation of fragment sizes as smaller particles are given a larger neighbor radius than what is physically correct. In this work, the neighbor radius is set to 70  $\mu\text{m}$ . This does exclude the possibility of finding two particles with radius greater than 35  $\mu\text{m}$  as neighbors. This should not be of great concern as the number of particles with radius greater than 35  $\mu\text{m}$  account for 2.3% of the total. The likelihood of two particles with this radius or greater to be neighbors is therefore relatively low. This method should give an appropriate estimate and reasonable information on the trend of fragmentation. The procedure of calculating the total fragmentation of the agglomerate begins with determination of the largest fragment in the system which is to be considered as the remaining structure from the initial agglomerate. The extent of fragmentation is then obtained by subtracting the number of particles in this fragment from the number of particles in the initial agglomerate.

### 3.5.7 Regime map

Moreno-Atanasio & Ghadiri (2006) derived a dimensionless number,  $\Delta$ , to characterize the strength of monodisperse agglomerates impacting a flat surface. If the energy required to break the contact between two particles is assumed to vary linearly with the kinetic impact energy an analytic expression for a dimensionless group is derived. However, because this derivation is based on a monodisperse system the analytical expression is not applicable for the polydisperse agglomerate as is. It is proposed that this number is extended for polydisperse agglomerates by integration of the bonding energy of each contact in the agglomerate and divide with the respective incident kinetic energy at each impact velocity. The essential meaning of the  $\Delta$  number is kept while its calculation procedure is tailored for the polydisperse system. Thus, the dimensionless number,  $\Delta$ , as will be used for the regime map is defined as:

$$\Delta = \frac{\text{Incident Kinetic Energy}}{\text{Agglomerate Bonding Energy}} = \frac{\sum_2^1 m_p v^2}{\sum E_{Bond}} \quad (67)$$

The bonding energy between two adhesive elastically deformable dry particles in equilibrium can be calculated from the JKR theory through equation 68 (Israelachvili, 2011):

$$E_{bond} = -0.6\pi a_0^2 W \quad (68)$$

where  $W$  is the interface energy and  $a_0$  is the equilibrium contact radius calculated by equation 15. Potential energy is stored as elastic deformation remaining at equilibrium and it will act to decrease the energy needed to separate the particles. The adhesive bonding energy is reduced by 40 % compared to the pure surface energy that would otherwise be needed to separate the two particles from each other (Israelachvili, 2011).

For wet contacts, the capillary force at contact is assumed to be independent of the overlap. The bonding energy is calculated by integration of the maximal capillary force over the equilibrium overlap,  $\delta$ , as shown in equation 69.

$$E_{bond} = dU = \int_0^{\delta} F_{cap} d\delta = \int_0^{\delta} 2\pi R_{eff} \gamma \cos(\theta_{eff}) d\delta = \dots$$

$$\dots 2\pi R_{eff} \gamma l \cos(\theta_{eff}) \delta \quad (69)$$

with the effective radius defined as the harmonic mean according to equation 45.

## 4. Results and discussion

The results from the wall-normal impact of wet and dry polydisperse agglomerates are analyzed and classified into several regimes according to their post impact behaviours. Subsequently, the plots of post impact equilibrium parameters are used to distinguish and characterize the impact behaviours. In this section, the identified impact regimes are described. The post impact equilibrium parameters including the damage ratio and broken initial bonds to measure how the structural integrity is preserved during the impact. Further measure of the strength of interparticle bonds is presented by the degree of fragmentation at the impact. The adhesiveness of the agglomerate is an important factor for the surface cleaning properties which will be presented by the capture ratio and total agglomerate-wall adhesion force. The result section is concluded by the creation of a regime map based on liquid content and the dimensionless  $\Delta$  number.

### 4.1 Impact regimes

Inspecting the simulation results, four impact regimes are identified. A general description and a representative picture of each impact regime will be presented in this section. It should be noted that the figures may have different length scales but to ease the comparison, the simulation box that is shown in all figures has a fixed size. Moreover, in figures to the left the view plane is tangential to the impact plane whereas, in figures to the right, the view plane is normal to the impact plane.

#### 4.1.1 Minor deformation

The first impact regime is found for lower  $\Delta$ -numbers and is characterized by the observation that both wet and dry agglomerates is only showing deformation and compaction. The structural integrity of the agglomerate is kept at impact such that the agglomerate is flattening and deforming against the impact surface as a single entity without any breakage or fragmentation. The interparticle bonding strength and viscous dissipation is great enough to consume the impact energy without any fragmentation. A representative example of this impact behaviour is shown in Figure 4:1.

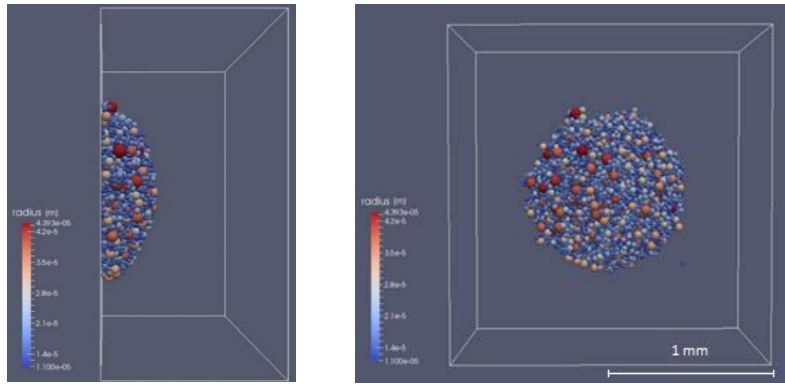


Figure 4.1. Representative impact behaviour of the deformation regime.

### 4.1.2 Major deformation, Minor fragmentation

The second impact regime is found in medium ranged  $\Delta$ -numbers. It is characterized by greater deformation and the onset of breakage and fragmentation. It is observed in figure 4:2 that the structure of the agglomerate is preserved although deformation and flattening occur to a larger extent compared to the first impact regime. Meanwhile, the agglomerate cannot fully dissipate the impact energy and some smaller fragments and single particles are found. Moreover, the edge of the impact surface is beginning to form strands resembling the beginning of possible fragments. A representative behaviour for this regime is shown in Figure 4:2.

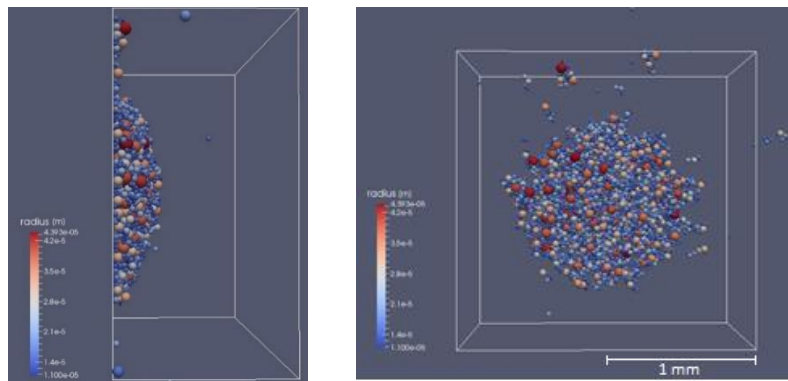


Figure 4.2. Representative impact behaviour of the major deformation, minor fragmentation regime.

### 4.1.3 Major deformation, Major fragmentation

The third regime is found for even larger  $\Delta$ -numbers. Characteristic of the impact behaviour in this regime is a significant deformation and major fragmentation. The structure of the agglomerate after the impact is more scattered and it is no longer one single, larger entity. It is

still possible to find a large fragment that can be regarded as the remaining structure of the initial agglomerate from which fragmentation and deformation is determined in relation to.

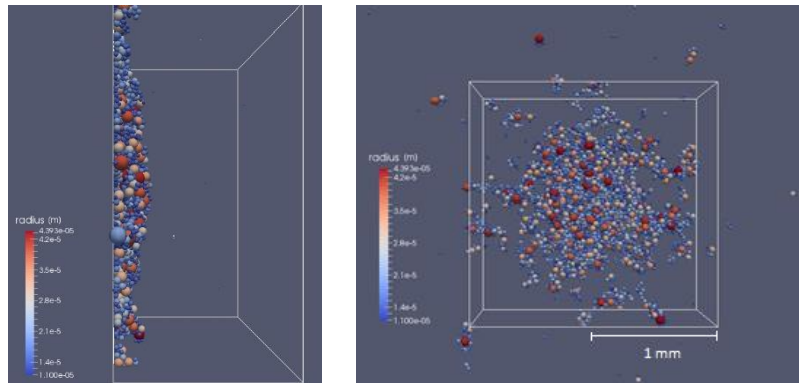


Figure 4.3. Representative impact behaviour of the major deformation, major fragmentation regime.

#### 4.1.4 Disintegration

For very large  $\Delta$ -numbers it is no longer applicable to describe the impact behaviour of the agglomerate as deformation. Many fragments of various sizes are found and it is no longer clear which fragment should constitute the main fragment corresponding to the deformed structure of the initial agglomerate. The number of small to medium sized fragments is increased and they are spread over a much greater area of the impact surface. A representative behaviour of this impact regime is shown in Figure 4:4.

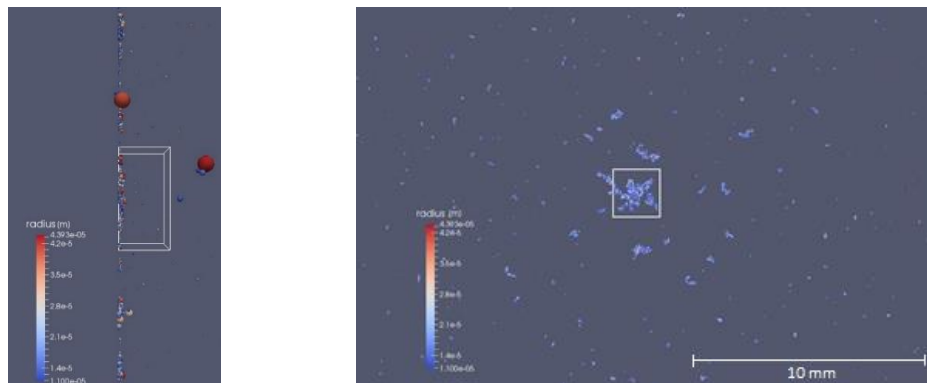


Figure 4:4. Representative impact behaviour of the disintegration regime.

## 4.2 Compactability and deformability

The strength of the agglomerate and thus the ability of an agglomerate to withstand impact without breaking is measured by the damage ratio and initial bonds broken at different liquid

contents and impact velocities. In Figure 4:5, the damage ratio and initial bonds broken are plotted against impact velocity for each liquid content. There is a sharp difference in the damage ratio between the dry and wet agglomerate conditions. At an impact velocity of 3 m/s, the damage ratio is significantly decreased, from -40 % in dry condition to around -13 % for the wet agglomerates. The negative value of the damage ratio implies that the number of bonds has increased compared to the initial state. This behaviour is explained by the mechanism of compaction and deformation that the agglomerate is subjected to during the impact. Particles are moving relative to each other and pressing against the wall resulting in a macroscopic deformation of the agglomerate structure. Particles which may previously not have been neighbors, can be brought into contact and form new bonds. The initial agglomerate is rather loose with a porosity of 52 % which further explain this behavior as a loose structure increase the likelihood and ability of the agglomerate to compact and deform during impact.

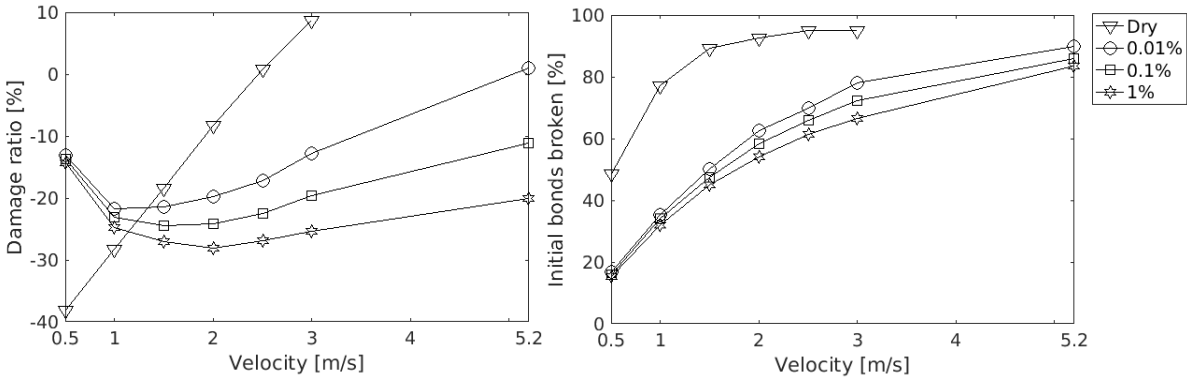


Figure 4.5. Left: Damage ratio (left) and initial bonds broken (right) as a function of velocity.

Looking at the wet agglomerates, the damage ratio decreases to a minimum value at a critical velocity. The absolute value of the minimum damage ratio and the velocity at which it occurs is shifted towards greater values with increasing liquid content. This is a clear example of the effect of the increased ranged capillary forces with liquid content. Even though the maximum capillary force is independent of liquid content, both the ranged interaction force and the rupture distance are increasing. The latter increase the agglomerates' strength which thus requires greater velocities to obtain maximum damage ratio. The absolute damage ratio is increased because the ability to withstand deformation and compaction is greater, allowing a denser, more structured arrangement and more bonds to be obtained. Increasing the impact velocity even further, the agglomerates cannot dissipate the repulsive force imparted at impact. This results

in an increased rate of bond breakage and therefore an increased damage ratio. As seen in Figure 4:5, after the minimum point, the damage ratio is increasing with velocity for all liquid contents and at a certain velocity the damage ratio is shifting sign. This shift from negative to positive damage ratio is found to occur at different velocities depending on the agglomerate condition. For the dry agglomerate, it occurs at a velocity of approximately 2.5 m/s and for agglomerates with 0.01% liquid content at approximately 5.2 m/s. This behaviour is expected to be found for all agglomerate liquid conditions. The reason why this is not seen for liquid content of 0.1% and 1% in Figure 4:5 is due to the increasing agglomerate strength with increasing liquid content. The simulated velocities are not imparting great enough force to produce this behaviour for these liquid contents.

There seems to be a noticeable difference in the behaviour of wet and dry agglomerates. The damage ratio is monotonically increasing with velocity for the dry agglomerate although the wet agglomerates show a minimum. Nonetheless, this is probably an apparent difference and it is in fact related to the simulated velocity range. In fact, the dry agglomerate should obey the same trend as the wet agglomerates with a minimum in the damage ratio at a certain velocity. However, as the dry agglomerate is weaker than the wet due to the very short ranged interaction of the van der Waals forces, which in the simulation is modelled as non-ranged interaction, the minimum of the dry agglomerate should be located at much lower velocities than the wet agglomerates. For instance, the damage ratio is theoretically zero at zero impact velocity implying that it cannot monotonically decrease by decreasing impact velocity. The latter fact would necessitate a minimum damage ratio in the range of 0-0.5m/s. Hypothetically, if simulations had been performed at impact velocities between 0-0.5 m/s a minimum would have been observed.

Looking at the rate of change of the damage ratio as a function of the impact velocity, the dry agglomerate is increasing its damage ratio with a much greater rate than any of the wet agglomerates does. This relates to the strength of the agglomerate and as expected it is found that even small amounts of liquid increase the strength significantly. At lower velocities, there is a great difference in the ratio of initial bonds broken between wet and dry agglomerates explaining the difference in the damage ratio. The wet agglomerates are showing the same trend as the dry with decreasing slope for increasing velocity.

### 4.3 Total fragmentation

In Table 4:1 the total number of fragmented particles in each of the simulated polydisperse agglomerate impacts is shown both in absolute numbers and in percentages of the total number of particles in the agglomerate. These values are determined by postprocessing the position data using DBSCAN. The total number of fragmented particles includes any particle found in a fragment and all single particles. In Table 4:2 the number of fragments are shown along with the sum of single particles and binary fragments within parenthesis.

*Table 4:1. Total number of fragmented particles for all simulated impact velocities and liquid contents. Numbers in parenthesis the percent of total number of particles.*

Impact Velocity	Dry	0.01%	0.1%	1%
0.5 m/s	1	-	-	-
1 m/s	103 (2.6)	-	-	-
1.5 m/s	1092 (27.3)	-	-	-
2 m/s	1541 (38.5)	8 (0.2)	-	-
2.5 m/s	2603 (65.0)	16 (0.4)	6 (0.15)	-
3 m/s	2780 (69.5)	124 (3.1)	56 (1.4)	2(0.05)
5.2 m/s	*	986 (24.6)	679 (16.9)	259 (6.475)

\* Velocity not simulated.

It is clearly seen the existence of critical impact velocities below which no fragmentation occurs for neither the wet nor the dry agglomerates. For lower velocities than these critical velocities only deformation and compaction occur while at the border, only few bonds are broken. Further increase in impact velocity results in greater total fragmentation as well as higher number of fragments. Comparing the wet agglomerates at the same impact velocity, both properties decrease with increasing liquid content. A clear observation of the increased strength of ranged capillary forces with increasing liquid content.

Table 4:2 Total number of fragments for all simulated impact velocities and liquid content. Numbers in parenthesis is the sum of single particles and particles in binary fragments.

Impact Velocity	Dry	0.01%	0.1%	1%
0.5 m/s	- (1)	-	-	-
1 m/s	4 (23)	-	-	-
1.5 m/s	27 (124)	-	-	-
2 m/s	62 (203)	- (8)	-	-
2.5 m/s	85 (308)	1 (13)	1 (3)	-
3 m/s	123 (431)	11 (30)	2 (13)	- (2)
5.2 m/s	*	54 (138)	29 (63)	17 (44)

\* Velocity not simulated

A further observation from the Table 4:1 is that the dry agglomerate changes impact behaviour with increasing velocity as seen in the difference in total fragmentation between 1 m/s (2.6%) and 1.5 m/s (27.3 %). On the contrary the wet agglomerates show a lower rate of increased fragmentation with velocity.

#### 4.4 Agglomerate-wall adhesion

When deforming against the wall, the agglomerate is spread out or flattened to some extent depending on the agglomerate strength. Another measure of deformation is therefore seen by the capture ratio, or the number of particles in immediate contact with the wall. In addition to the capture ratio it is of interest to determine the total adhesive force between the agglomerate and the wall after impact. This parameter is of greater interest for the surface cleaning properties. In Figure 4:6 capture ratio and total adhesive force is plotted as a function of the impact velocity for each liquid content.

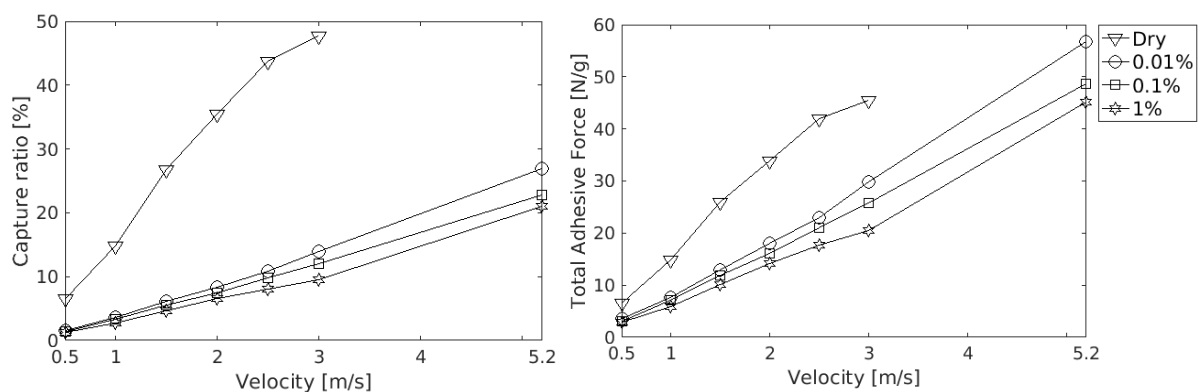


Figure 4:6. Capture ratio (left) and total adhesive force (right) as a function of liquid content.

It is seen that the capture ratio is strictly increasing with velocity at all conditions. This is to be expected as the capture ratio should follow the extent of deformation. Even though the damage ratio is showing a minimum, the capture ratio does not. Looking at the dry agglomerate it is following the trend of initial bonds broken ratio seen in Figure 4:5 with a linear increase at lower velocity and a decreasing slope at higher velocities, reaching an asymptotic behaviour. The wet agglomerates are increasing linearly for all velocities with no asymptotic behaviour. Comparing to their respective initial bonds broken ratio, they are following the same trend albeit showing a somewhat decreasing slope between 3 m/s and 5.2 m/s. At lower impact velocities energy is quickly dissipated by all liquid contents and they only show minor deformation as seen by the low values of initial bonds broken and damage ratio in Figure 4:5.

The difference in strength between liquid contents is represented more with increased impact velocities as the work needed to dissipate the impact energy is increased. Increasing liquid content would increase the rupture distance and the capillary force, thus increasing the ability to deform without as much fragmentation at a given velocity. Looking at deformation and capture ratios at any given velocity there is not a great difference between liquid contents. What is found is a slightly increased difference in the capture ratios with velocity. Comparing the total fragmentation, shown in Table 4:1, between liquid contents for the same impact velocity the trend is an increasing difference with velocity as well.

Inspecting only the capture ratio of the dry agglomerate would seem to show much greater adhesive force than the wet agglomerate since plenty more particles are contacting the surface. The actual adhesive force is calculated and plotted in Figure 4:6 and it is found that the difference is not as great as could be expected. The dry agglomerate does indeed show greater total force for all comparable impact velocities. However, for example for the impact at 3 m/s, the dry agglomerate shows a total adhesive force of 45 [ $N/g$ ] while the value for the wet agglomerates ranges between 28-18 [ $N/g$ ]. Meanwhile, the difference in capture ratio is 49% to 12-9%. This can be explained by the fact that the maximal capillary force between any particle and the wall is approximately twice as great as the pull-off force for the same dry particle-wall interaction, compare equation 61 and 69.

## 4.5 Regime map

To construct the regime map, suitable criteria to distinguish the regimes must be determined. The identified impact regimes are most easily characterized by the total fragmentation. The border between any two regimes is not abrupt but is rather a smooth transition. The criterion is set as a value that should best represent the transition. For example, comparing the representative behaviour of the two regimes in Figure 4:1 and Figure 4:2, it is seen that in the minor deformation regime the agglomerate is keeping the circular shape around the edge of the impact surface, whereas in the major deformation, minor fragmentation regime, the shape is no longer circular, there are some number of fragmented particles and there are potential groups or strands of particles around the edge. Therefore, the border of the two regimes is gliding as the smooth transition from the minor deformation regime into showing fragmentation and breakage. Still, only a small amount of fragmentation is necessary for the distinction between them and an appropriate value of the border is found to be total fragmentation of 3%.

In the same manner the transition, between major deformation, minor fragmentation and major deformation, major fragmentation is smooth and the border is chosen to be the total fragmentation of 20%. It should be noted that the major deformation, major fragmentation regime is in fact not observed for the 0.1% and 1% liquid content. However, it is observed for the 0.01% liquid condition and the regimes are thought to be universal for all liquid contents because they show the same trend in all the studied parameters including damage ratio, initial bonds broken, capture ratio and total fragmentation. The simulation velocity range is thus too narrow for the higher liquid contents to show this impact behaviour. The disintegration regime is only shown by the dry agglomerate in the simulation. But again, because of the similarity in behaviour it is expected to be shown by wet agglomerates at increased velocities. Over 50% fragmentation is considered as the border to the disintegration regime. The regime map is displayed in Figure 4:7. In the construction of the regime map, the borders were drawn by linear interpolation of total fragmentation results.

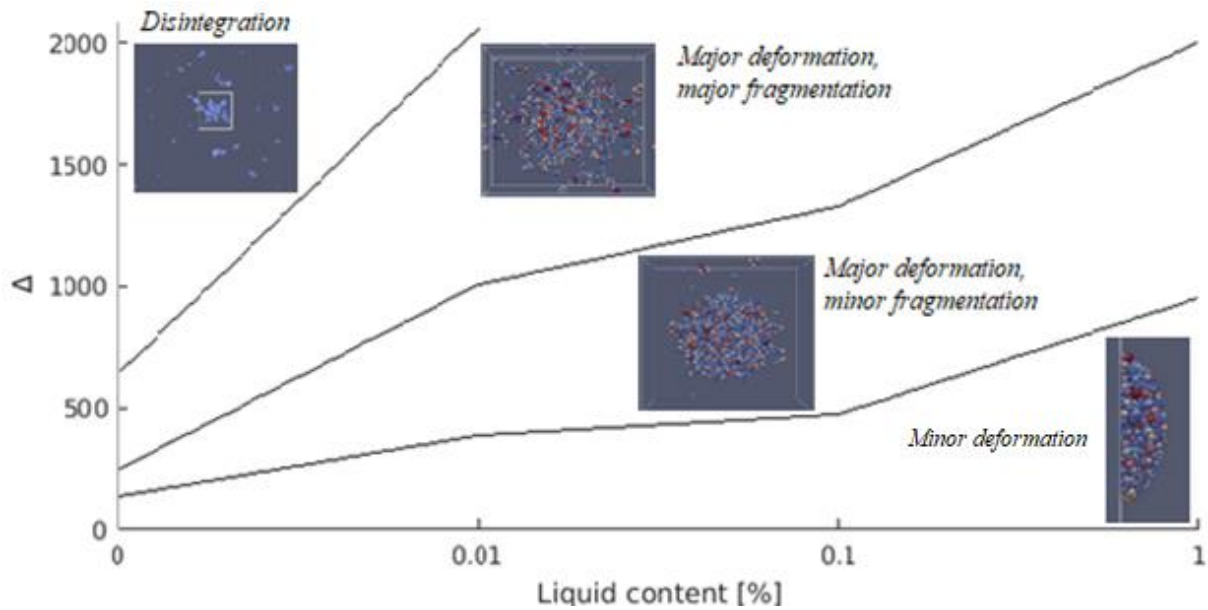


Figure 4:7. Regime map relating liquid content and  $\Delta$  number to the impact behaviour of wet and dry agglomerates.

## 4.6 Reflections

In this thesis, the impact behaviour of wet and dry polydisperse agglomerates was investigated. A regime map was constructed as a guide to show the impact regimes as a function of impact velocity and agglomerate liquid content. A methodology is developed, producing a regime map, describing the impact behaviour of wet and dry agglomerates based on properties that are known a priori to the impact simulation. As such it can be used as a tool to predict impact properties for a given agglomerate condition. Cleaning properties such as capture ratio and total adhesive force is easily obtained output parameters from the model and can be included in the regime map. This could be used in the development of cleaning systems by using it to determine boundary conditions for dirt agglomerates through look-up tables of parameters pertaining to cleaning properties such as the total adhesive force and capture ratio. It also possible to extract further information affecting the cleaning properties such as the three-dimensional structure of adhered particle layers or local density differences.

## 5. Conclusions

Analysis of impact results show the existence of four impact regimes. Three of the impact regimes were observed for both wet and dry agglomerate impacts while the fourth regime, disintegration, was only observed for dry agglomerate impacts. The impact regimes are found to be universal for both wet and dry agglomerates. Liquid content is found to have a large effect on the strength of the agglomerate because both the ranged capillary force and the bridge rupture distance is increasing with liquid content. This explains the observation that the regime transitions occur at higher velocities with increasing agglomerate liquid content. This is further substantiated by analysis of damage ratio, initial bonds broken and total fragmentation. It is found that the behavior of each measure is the same for all liquid contents, but the absolute values for a given impact velocity increases with liquid content.

## **6. Suggestions for further work**

To further enhance the accuracy of the regime map in terms of post impact equilibrium parameter values, and to determine precise regime borders, it is necessary to specify the system of interest and obtain more exact material properties. The regime map can be expanded further by including other impact conditions such as for example the impact angle. Moreover, further simulations should be conducted with liquid content up to approximately 10% such that the regime map is spanning the full pendular liquid bridge regime. As not all regimes were observed for the wet agglomerates further simulations should also be conducted at greater impact velocities to allow for the observation of all regimes. It was found that even small changes in liquid bridge volume is important for the size of the ranged capillary force and rupture distance and thus the agglomerate strength. Further work on the DEM model should therefore be aimed at implementing improved theories of liquid contribution at bridge formation as well as distribution at bridge rupture.

## References

- BUTT, H.-J. & KAPPL, M. 2010. *Surface and Interfacial Forces*, Wiley-VCH Verlag GmbH & Co. KGaA.
- CROW, C. T., SCHWARZKOPF, J. D., SOMMERFELD, M. & TSUJI 2011. *Multiphase Flows with Droplets and Particles*. Second Edition ed.: CRC Press.
- DE LAZZER, A., DREYER, M. & RATH, H. J. 1999. Particle–Surface Capillary Forces. *Langmuir*, 15, 4551-4559.
- DERJAGUIN, B. V., MULLER, V. M. & TOPOROV, Y. P. 1975. Effect of contact deformations on the adhesion of particles. *Journal of Colloid and Interface Science*, 53, 314-326.
- ESTER, M., KRIEGEL, H.-P., SANDER, J. & XU, X. 1996. A density-based algorithm for discovering clusters a density-based algorithm for discovering clusters in large spatial databases with noise. *Proceedings of the Second International Conference on Knowledge Discovery and Data Mining*. Portland, Oregon: AAAI Press.
- FISHER, L. R. & ISRAELACHVILI, J. N. 1981. Direct measurement of the effect of meniscus forces on adhesion: A study of the applicability of macroscopic thermodynamics to microscopic liquid interfaces. *Colloids and Surfaces*, 3, 303-319.
- FISHER, R. A. 1926. On the capillary forces in an ideal soil; correction of formulae given by W. B. Haines. *The Journal of Agricultural Science*, 16, 492-505.
- GAYLARD, A. P., KIRWAN, K. & LOCKERBY, D. A. 2017. Surface contamination of cars: a review. *Proceedings of the Institution of Mechanical Engineers, Part D: Journal of Automobile Engineering*, 0954407017695141.
- HAGEMEIER, T., HARTMANN, M. & THÉVENIN, D. 2011. Practice of vehicle soiling investigations: A review. *International Journal of Multiphase Flow*, 37, 860-875.
- HOPPE, R. 1970. The Coordination Number – an “Inorganic Chameleon”. *Angewandte Chemie International Edition in English*, 9, 25-34.

ISRAELACHVILI, J. 1992. Intermolecular and Surface forces, ACADEMIC PRESS LIMITED.

ISRAELACHVILI, J. N. 2011. 17 - Adhesion and Wetting Phenomena. Intermolecular and Surface Forces (Third Edition). Boston: Academic Press.

JOHNSON, K. L., KENDALL, K. & ROBERTS, A. D. 1971. Surface Energy and the Contact of Elastic Solids. Proceedings of the Royal Society of London. Series A, Mathematical and Physical Sciences, 324, 301-313.

JORDAN, D. W. 1954. The adhesion of dust particles. British Journal of Applied Physics, 5, S194.

KETTERHAGEN, W. R., AM ENDE, M. T. & HANCOCK, B. C. 2009. Process modeling in the pharmaceutical industry using the discrete element method. Journal of Pharmaceutical Sciences, 98, 442-470.

KHALILITEHRANI, M. 2016. A multiscale approach to particulate flows in dense high-shear systems. Doctorate, Chalmers University of Technology.

KRIJT, S., GÜTTLER, C., HEIßELMANN, D., DOMINIK, C. & TIELENS, A. G. G. M. 2013. Energy dissipation in head-on collisions of spheres. Journal of Physics D: Applied Physics, 46, 435303.

KRUGGEL-EMDEN, H., SIMSEK, E., RICKELT, S., WIRTZ, S. & SCHERER, V. 2007. Review and extension of normal force models for the Discrete Element Method. Powder Technology, 171, 157-173.

LAMBERT, P. & VALSAMIS, J.-B. 2013. Axial Capillary Forces. In: LAMBERT, P. (ed.) Surface Tension in Microsystems: Engineering Below the Capillary Length. Berlin, Heidelberg: Springer Berlin Heidelberg.

LI, Q., RUDOLPH, V., WEIGL, B. & EARL, A. 2004. Interparticle van der Waals force in powder flowability and compactibility. International Journal of Pharmaceutics, 280, 77-93.

- LIAN, G., THORNTON, C. & ADAMS, M. J. 1993. A Theoretical Study of the Liquid Bridge Forces between Two Rigid Spherical Bodies. *Journal of Colloid and Interface Science*, 161, 138-147.
- LIAN, G., THORNTON, C. & ADAMS, M. J. 1998. Discrete particle simulation of agglomerate impact coalescence. *Chemical Engineering Science*, 53, 3381-3391.
- MARSHALL, J. & LI, S. 2014. *Adhesive Particle Flow - A Discrete Element Approach*, Cambridge University Press.
- MIKAMI, T. 1998. Numerical simulation of cohesive powder behaviour in a fluidized bed. *Chemical Engineering Science*, 53, 1927-1940.
- MINDLIN, R. D. 1949. Compliance of elastic bodies in contact. *Journal of applied mechanics*, 16, 259-268.
- MITARAI, N. & NORI, F. 2006. Wet granular materials. *Advances in Physics*, 55, 1-45.
- MORENO-ATANASIO, R. & GHADIRI, M. 2006. Mechanistic analysis and computer simulation of impact breakage of agglomerates: Effect of surface energy. *Chemical Engineering Science*, 61, 2476-2481.
- MÖRTSTEDT, S.-E. & HELLSTEN, G. 2012. *Data och Diagram*, LIBER.
- NAKAMURA, H., FUJII, H. & WATANO, S. 2013. Scale-up of high shear mixer-granulator based on discrete element analysis. *Powder Technology*, 236, 149-156.
- NASE, S. T., VARGAS, W. L., ABATAN, A. A. & MCCARTHY, J. J. 2001. Discrete characterization tools for cohesive granular material. *Powder Technology*, 116, 214-223.
- NGUYEN, D., RASMUSON, A., THALBERG, K. & NIKLASSON BJÖRN, I. 2014. Numerical modelling of breakage and adhesion of loose fine-particle agglomerates. *Chemical Engineering Science*, 116, 91-98.
- OLIVER, W. C. & PHARR, G. M. 1992. An improved technique for determining hardness and elastic modulus using load and displacement sensing indentation experiments. *Journal of Materials Research*, 7, 1564-1583.

PITOIS, O., MOUCHERONT, P. & CHATEAU, X. 2000. Liquid Bridge between Two Moving Spheres: An Experimental Study of Viscosity Effects. *Journal of Colloid and Interface Science*, 231, 26-31.

POWDER TECHNOLOGY INC. 2016. *Arizona Test Dust (ATD) Safety Data Sheet* [Online]. Available:<http://www.powdertechologyinc.com/wp-content/uploads/2012/08/SDS.01.Arizona-Test-Dust.4-Feb-2016.pdf> [Accessed 1 Feb 2017].

RABINOVICH, Y. I., ADLER, J. J., ESAYANUR, M. S., ATA, A., SINGH, R. K. & MOUDGIL, B. M. 2002. Capillary forces between surfaces with nanoscale roughness. *Advances in Colloid and Interface Science*, 96, 213-230.

RABINOVICH, Y. I., ESAYANUR, M. S. & MOUDGIL, B. M. 2005. Capillary Forces between Two Spheres with a Fixed Volume Liquid Bridge: Theory and Experiment. *Langmuir*, 21, 10992-10997.

REAGLE, C. J., DELIMONT, J. M., NG, W. F., EKKAD, S. V. & RAJENDRAN, V. P. 2013. Measuring the coefficient of restitution of high speed microparticle impacts using a PTV and CFD hybrid technique. 24.

SHAMY, U. E. & GRÖGER, T. 2008. Micromechanical aspects of the shear strength of wet granular soils. *International Journal for Numerical and Analytical Methods in Geomechanics*, 32, 1763-1790.

SHANMUGAM, S. 2015. Granulation techniques and technologies: recent progresses. *BioImpacts : BI*, 5, 55-63.

SHI, D. L. & MCCARTHY, J. J. 2008. Numerical simulation of liquid transfer between particles. *Powder Technology*, 184, 64-75.

TAMADONDAR, M. R., RASMUSON, A., THALBERG, K. & NIKLASSON BJÖRN, I. 2017. Numerical modeling of adhesive particle mixing. *AIChE Journal*, 63, 2599-2609.

THORNTON, C. 2015. *Granular Dynamics, Contact Mechanics and Particle System Simulation*. Springer International Publishing.

- THORNTON, C. & LIU, L. 2004. How do agglomerates break? *Powder Technology*, 143, 110-116.
- WEI, M., BOWMAN, R. S., WILSON, J. L. & MORROW, N. R. 1993. Wetting Properties and Stability of Silane-Treated Glass Exposed to Water, Air, and Oil. *Journal of Colloid and Interface Science*, 157, 154-159.
- WEIR, G. & TALLON, S. 2005. The coefficient of restitution for normal incident, low velocity particle impacts. *Chemical Engineering Science*, 60, 3637-3647.
- WILLETT, C. D., ADAMS, M. J., JOHNSON, S. A. & SEVILLE, J. P. K. 2000. Capillary Bridges between Two Spherical Bodies. *Langmuir*, 16, 9396-9405.
- YANG, Q. J. & ZHAO, C. F. 2014. DEM analysis of geomechanical behaviour of methane hydrate-bearing sediments. *Geomechanics from Micro to Macro*. CRC Press.
- YOSHIDA, M., YAMATANI, A. & CHINA, H. 1998. Prediction of dirt contamination on vehicle body surface. *JSAE Review*, 19, 257-262.

## Appendix A

Calculated values of formation distance and rupture distance for the extreme cases of particle-particle and particle-wall interactions are shown in the following tables.

### Appendix A.1

#### Bridge formation distance particle-particle interaction

Formation distance for particle-wall interaction is the same as the cut-off distance,  $\delta_f$ , for a single particle

<b>Liquid content 0.01%</b>		
<b>Radius [<math>\mu\text{m}</math>]</b>	<b><math>\delta_f</math> [nm]</b>	<b><math>\delta_f / R_{\text{eff}}</math> [%]</b>
11	0.366	0.0033
44	1.47	0.0033
11-44	1.836	0.0167 (of smaller particle)
<b>Liquid content 0.1%</b>		
<b>Radius [<math>\mu\text{m}</math>]</b>	<b><math>\delta_f</math> [nm]</b>	<b><math>\delta_f / R_{\text{eff}}</math> [%]</b>
11	3.66	0.033
44	14.7	0.033
11-44	18.36	0.167 (of smaller particle)
<b>Liquid content 1%</b>		
<b>Radius [<math>\mu\text{m}</math>]</b>	<b><math>\delta_f</math> [nm]</b>	<b><math>\delta_f / R_{\text{eff}}</math> [%]</b>
11	36.5	0.333
44	146e	0.333
11-44	182.5	1.66 (of smaller particle)

## Appendix A.2

### Bridge rupture distance particle-wall interaction

<b>Liquid content 0.01%</b>	
<b>Radius [<math>\mu\text{m}</math>]</b>	<b>Rupture distance / <math>R_{\text{eff}}</math> [%]</b>
11	2.06
44	2.06
<b>Liquid content 0.1%</b>	
<b>Radius [<math>\mu\text{m}</math>]</b>	<b>Rupture distance / <math>R_{\text{eff}}</math> [%]</b>
11	4.39
44	4.39
<b>Liquid content 1%</b>	
<b>Radius [<math>\mu\text{m}</math>]</b>	<b>Rupture distance / <math>R_{\text{eff}}</math> [%]</b>
11	9.26
44	9.26

## Appendix A.3

### Bridge rupture distance particle-particle interaction

<b>Liquid content 0.01%</b>	
<b>Radius [<math>\mu\text{m}</math>]</b>	<b>Rupture distance / <math>R_{\text{eff}}</math> [%]</b>
11 - 11	5.368
44 - 11	16.304 (of smaller particle)
44 - 44	5.368
<b>Liquid content 0.1%</b>	
<b>Radius [<math>\mu\text{m}</math>]</b>	<b>Rupture distance / <math>R_{\text{eff}}</math> [%]</b>
11 - 11	11.63
44 - 11	33.96 (of smaller particle)
44 - 44	11.63
<b>Liquid content 1%</b>	
<b>Radius [<math>\mu\text{m}</math>]</b>	<b>Rupture distance / <math>R_{\text{eff}}</math> [%]</b>
11 - 11	25.38
44 - 11	88 (of smaller particle)
44 - 44	25.38